The symphony of pulsations and binarity among massive stars using HERMES spectroscopy and TESS photometry

K. Thomson-Paressant[1]★, D. M. Bowman[1,2], L. J. A. Scott[1], F. Nardini[1], J. Bodensteiner[3], T. Shenar[4], L. Mahy[5], G. Handler[6], N. Shitrit[4], I. Arcavi[4], M. Abdul-Masih[7,8], S. Simon-Diaz[7,8], P. Van Daele[1], A. J. Kalita[1], L. Dennis[1], J. Henneco[1], A. Tkachenko[2], H. Sana[2,9], H. Van Winckel[2]

[1] *School of Mathematics, Statistics and Physics, Newcastle University, Newcastle upon Tyne, NE1 7RU, United Kingdom*
[2] *Institute of Astronomy, KU Leuven, Celestijnenlaan 200D, 3001 Leuven, Belgium*
[3] *Anton Pannekoek Institute for Astronomy, University of Amsterdam, Science Park 904, 1098 XH Amsterdam, the Netherlands*
[4] *School of Physics and Astronomy, Tel Aviv University, Tel Aviv 6997801, Israel*
[5] *Royal Observatory of Belgium, Avenue Circulaire/Ringlaan 3, B-1180 Brussels, Belgium*
[6] *Nicolaus Copernicus Astronomical Center, Polish Academy of Sciences, ul. Bartycka 18, PL-00-716 Warszawa, Poland*
[7] *Instituto de Astrofisica de Canarias, C. Via Lactea, s/n, 38205 La Laguna, Santa Cruz de Tenerife, Spain*
[8] *Universidad de La Laguna, Dpto. Astrofisica, Av. Astrofsico Francisco Sanchez, 38206 La Laguna, Santa Cruz de Tenerife, Spain*
[9] *Leuven Gravity Institute, KU Leuven, Celestijnenlaan 200D, 3001 Leuven, Belgium*

Accepted XXX. Received YYY; in original form ZZZ

ABSTRACT

There is a wide range of variability mechanisms among intermediate mass and massive stars, which are not yet fully understood. Using multiple complementary data sources for a large population of B- and O-type stars, we aim to study the prevalence and interplay of different types of variability, including binarity, pulsation, and rotation, to prepare for future modelling. To this end, we analyse high-resolution HERMES spectra and 2-min cadence TESS photometry and characterise the diverse variability observed within a population of 873 O- and B-type stars. The spectroscopic data were normalised using machine-learning techniques, compared to a grid of synthetic TLUSTY spectra to determine stellar parameters, and used to identify radial velocity variability across multiple epochs. Photometric time series were analysed using standard frequency analysis methods to detect pulsations and rotational modulation signatures. We find that more than 93 per cent of the sample exhibits photometric variability. Photometric variability caused by pulsations is identified in 82 per cent of the sample, with dominant contributions from β Cep and slowly pulsating B-type stars, as well as stochastic low-frequency variability. Moreover, approximately 17 per cent of the stars show evidence of binarity, including both eclipsing and spectroscopic systems, although the latter is a lower limit owing to the limited number of spectroscopic epochs. We also identify candidates exhibiting rotational modulation, suggestive of large-scale strong magnetic fields. This work represents one of the largest homogeneous surveys of variability for intermediate-mass and massive stars in the Northern hemisphere, combining both photometry and spectroscopy, and complementing similar efforts in the Southern hemisphere. It provides a statistical framework for future studies of stellar structure and evolution, particularly in the context of asteroseismology.

Key words: asteroseismology - stars: binaries: spectroscopic - stars: binaries: eclipsing - stars: early-type - stars: evolution - stars: rotation

1 INTRODUCTION

Intermediate- and high-mass stars play a fundamental role in stellar and galactic evolution, spanning regimes that contribute both to local stellar physics and to the large-scale evolution of galaxies. Through their intense radiation fields, strong stellar winds, and dramatic deaths as supernovae or gamma-ray bursts they greatly impact their environment (Bromm & Larson 2004). The heavier elements they produce in their cores, which are then distributed via mass loss or via explosive events at the ends of their lives, are a major contributor to chemical enrichment, which can both inhibit or promote the formation of new generations of stars (Massey 2003; Langer 2012). Finally, as the progenitors of both black holes and neutron stars, whose merger events produce gravitational waves, massive stars shed new light on the structure and expansion of the cosmos, and allow for the testing of novel physical prescriptions for gravity (e.g. Abbott et al. 2017b,a; Laplace et al. 2020). While the most massive stars dominate feedback through winds and explosive endpoints, intermediate-mass stars provide an important link between low- and high-mass stellar structure regimes. In particular, stars in the late-B and A spectral range exhibit a transition in internal structure and variability properties, making them valuable laboratories for studying transport processes,

★ E-mail: Keegan.Thomson-Paressant@newcastle.ac.uk

pulsation driving, rotation, and magnetism across the upper main sequence (Aerts 2021; Bowman 2020; Kurtz 2022).

Intermediate- and high-mass stars are governed by a complex interplay of several physical processes such as convection, rotation, mixing, magnetic fields, and mass loss, many of which remain imperfectly understood. As such, acquiring a greater knowledge of each of these processes is essential, not only for achieving a better picture of the life cycles of intermediate- and high-mass stars, but also for informing our broader understanding of stellar structure and evolution across the Hertzsprung–Russell (HR) diagram (Meynet & Maeder 2000; Aerts 2021; Kurtz 2022).

Binarity plays a key role in the evolution of stars (e.g. Sana et al. 2012; de Mink et al. 2013), altering their internal structure, angular momentum evolution, evolutionary pathways, and end products through processes such as tidal interactions, mass transfer, and mergers (see Langer 2012; Marchant & Bodensteiner 2024, for reviews). Pulsating eclipsing binaries in particular represent some of the best laboratories for improving stellar evolution theory (see Southworth & Bowman 2025, for a review). Observational studies of O- and B-star populations have demonstrated that multiplicity is extremely common, with inferred binary fractions ranging from approximately 25 to 80 per cent in O- and B-type stars depending on stellar mass, orbital separation sensitivity, and the properties of the parent population (e.g. Moe & Di Stefano 2017; Offner et al. 2023). For example, studies of early B-type stars in galactic open clusters reveal high multiplicity fractions ($\geq$ 50 per cent) and a significant population of close binaries (Banyard et al. 2022; Frost et al. 2025; Nardini et al. 2025). Surveys at subsolar metallicity, such as in the LMC, report similarly elevated binary fractions ($\geq$ 60 per cent) among massive stars (Sana et al. 2012, 2013, 2025; Villaseñor et al. 2025; Dunstall et al. 2015). These results indicate that binarity is not only prevalent but also a fundamental characteristic of massive-star populations across a wide range of environments. Consequently, accurately identifying and characterising binary systems is essential for interpreting observed stellar properties, disentangling binarity-induced variability from intrinsic stellar phenomena, and placing meaningful constraints on stellar evolution models (see Southworth & Bowman 2025).

One of the most informative methods for probing the physics of stars is through the study of their variability. Variations in brightness and spectral lines arise from a variety of mechanisms, including binarity, rotational modulation, pulsation, mass loss, and magnetic activity. Each of these processes offers insight into different layers or aspects of a star's structure. This is particularly true across the B-star regime, where pressure modes, gravity modes, and rotational variability coexist and probe different regions of stellar interiors, enabling comparisons across stellar mass and evolutionary state (Aerts et al. 2010; Bowman 2020). Traditional observational methods, such as photometry and high-resolution spectroscopy, have long enabled the detection and characterisation of these phenomena. More recently, the study of stellar oscillations via asteroseismology (see Aerts et al. 2010) has emerged as a powerful tool to investigate internal stellar structure and infer stellar parameters with unprecedented precision — see review by Kurtz (2022). Thanks to recent space-based missions such as the Convection, Rotation and planetary Transits (CoRoT; Auvergne et al. 2009) satellite, *Kepler* (Borucki et al. 2010), and the Transiting Exoplanet Survey Satellite (TESS; Ricker et al. 2015), our ability to utilise this technique has been greatly expanded (see reviews by Chaplin & Miglio 2013; Hekker & Christensen-Dalsgaard 2017; Bowman 2020; Aerts 2021).

In this study, we have performed a combined photometric and spectroscopic analysis of 873 O- and B-type stars in the Northern hemisphere, using recent TESS space mission light curves and multi-epoch high-resolution spectra from HERMES at the Mercator telescope (Section 2). We present here the demographics of variability caused by pulsations and binarity displayed in the sample determined using both photometry and spectroscopy (Section 3). A few studies of smaller samples have been performed previously for massive stars in the Southern hemisphere (e.g. Burssens et al. 2020), and so in this work we complement this with a (much larger) sample of OB-type stars in the Northern hemisphere. The goal of this work is to identify stars with variability caused by pulsations (Section 4), binarity (Section 5), as well as candidate magnetic stars based on rotational modulation (Section 6), which in future work can be studied using binary modelling (e.g. Zapartas et al. 2026), in-depth magnetic characterisation (e.g. Erba et al. 2024), and forward asteroseismic modelling (e.g. Burssens et al. 2023; Vanlaer et al. 2025; Fritzewski et al. 2025).

2 DATA ANALYSIS

2.1 Target selection

At the inception of this project, we used SIMBAD (Wenger et al. 2000) to construct a sample of 4121 stars with a spectral type of O or B and bright enough (i.e. $V \leq 14$ mag) to prepare a series of TESS Guest Investigator (GI[1]) proposals throughout cycles 3-8. These targets are typically located in star-forming regions in the Milky Way. However, the sampling of the sky by the TESS mission is not regular nor uniform. In cycles 1 and 2 (2018-07-25 to 2020-07-04), TESS observed 13 sectors (each lasting 28 d) in each ecliptic hemisphere using four cameras with a combined field of view of $24 \times 96°$. In cycles 3 and 4 (2020-07-05 to 2022-09-01), TESS observed 13 sectors in the South, 11 in the North, and a further 5 sectors covering the ecliptic plane itself. In cycles 5 and 6 (2022-09-01 to 2024-10-01) TESS covered 9 southern sectors, 16 Northern sectors, and 3 ecliptic sectors. Cycle 7 (2024-10-01 to 2025-09-15) covered 3 Northern, 2 ecliptic and 8 southern sectors, and cycle 8 is currently ongoing and due to end on 2026-09-07.

Due to the evolution of observing strategy over the course of the TESS mission, the cadence and duration of the assembled light curves is star dependent. For example, some stars have continuous light curves spanning up to 1 yr because they lie in one of the continuous viewing zones (see Ricker et al. 2015), whereas the majority of stars only have 1 sector of TESS data in each cycle (approximately 27 d). From the large sample of 4121 OB-type stars with $V < 14$ mag, a total of 2248 were selected to be observed with a short cadence of 2 min in the context of several successful GI proposals[2].

2.2 HERMES spectroscopic data

To complement the TESS observations, we initiated a large spectroscopic follow-up programme with the 1.2-m Mercator telescope[3], which is located on La Palma, Spain. The latitude and technical specifications of the observatory imposed a brightness requirement of $V < 12$ mag and restrictions to targets mostly in the Northern hemisphere (i.e. $\delta > -30°$). We also removed any stars from the follow-up programme that already had previous observations in the Mercator

[1] https://heasarc.gsfc.nasa.gov/docs/tess/approved-programs.html
[2] proposal IDs: G03059, G04074, G05036, G06037, and G07037 (PI: Bowman).
[3] https://www.mercator.iac.es/instruments/

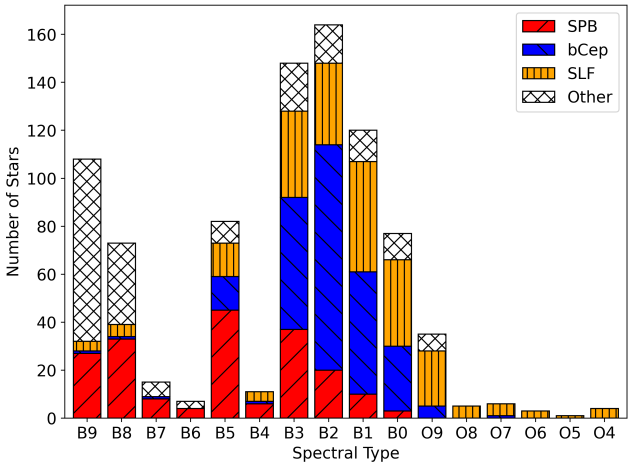

Figure 1. Distribution of spectral types from SIMBAD for the stars in our sample, classified by pulsator class from our analysis of TESS photometry, described in detail in Section 2.4.

archive. The large programme with the Mercator telescope to assemble these spectra ran between 2022-2025 (programme ID 123; PI: Bowman). The final sample presented and analysed in this paper with TESS data and new Mercator spectra is 873 stars.

The spectroscopic data in this work were assembled with the High Efficiency and Resolution Mercator Echelle Spectrograph (HERMES; Raskin et al. 2011; Raskin & Van Winckel 2014). The HERMES instrument is a fibre-fed prism-cross-dispersed echelle spectrograph based on a white-pupil design, a CCD with 2048×4608 pixels, and covers the 3800-9000 Å wavelength range with a resolving power of R = 85000 (Raskin et al. 2011; Raskin & Van Winckel 2014). The spectra were reduced by the HERMES data reduction software (HERMES-DRS, v.7.0), which includes bias and dark correction, flat-fielding, wavelength calibration, cosmic ray removal, and correction for barycentric motion.

The goal of our spectroscopic programme was to acquire three epochs per star, two separated by 1-2 months and a third occurring about a year later. Thus, both short- and long-period radial velocity variability should be detectable. Of the 873 stars in our sample, 138 successfully fulfilled these criteria (with a further 32 that have at least 3 spectra but do not fulfil the scheduling criteria), 464 targets have two out of three epochs requested, and 409 targets have only a single epoch to date. Nonetheless, we retain the entire sample of 873 stars for spectroscopic analysis.

2.2.1 *Visual inspection to identify SB2s and emission line stars*

The reduced HERMES spectra were assessed to look for a variety of features, including spectral line variability, chemical peculiarity, binarity, and emission features. We first visually inspected the regions corresponding to Hα and He I lines at 6563 and 6678 Å, respectively, to look for emission features typical of either OBe stars or blue supergiants (BSG). We simultaneously sought to identify double-lined spectroscopic binary (SB2) systems as, together with the emission-line stars, these targets would need to be treated differently in the following steps. For completeness, we also compared our sample with the 'SBX' database of spectroscopic binaries (Pourbaix et al. 2004; Merle et al. 2026), and took note of any overlap. This database does not explicitly classify targets as either SB1 or SB2, but we took note of the 38 targets that were included in SBX for the future analysis steps.

Inspection of the data resulted in the identification of 19 SB2 systems, 128 OBe stars, and 26 BSGs (determined through a combination of P Cygni-like emission features in the Hα line region and the spectral type provided from SIMBAD). This leaves us with 700 non-emission line and non-SB2 stars for subsequent analysis. We leave the analysis of emission-line stars and SB2 systems for future work.

2.2.2 *Normalisation*

After having identified and separated emission-line stars and SB2 systems out from the sample, we normalised all the remaining spectra. Instead of performing normalisation manually on a star-by-star and spectrum-by-spectrum basis, the HERMES spectra were continuum normalised automatically utilising the SUPPNet[4] software package (Różański et al. 2022). SUPPNet is a neural network designed to predict the location of the pseudo-continuum in stellar spectra, having been trained on both synthetic and real spectra of stars spanning the O to G spectral types, and with a wide range of variability included (e.g. pulsation, chemical peculiarity, and emission features).

2.2.3 *Cross correlation*

After normalisation, next we followed the procedure presented in Shenar et al. (2019), Dsilva et al. (2020), and Nardini et al. (2025), which was adapted from Zucker et al. (2003), and performed a cross-correlation technique on the continuum-normalised spectra for each star. Using a set of spectral lines as reference points, the spectra were co-added and weighted based on their respective signal-to-noise ratios (S/N). To this end, we utilised the He I absorption lines located at 4472, 5876, and 6678 Å as the reference points to anchor the cross-correlation across all the epochs available for a given star. The benefits of this cross-correlation process are two-fold: (i) it can be used to determine the reference point for calculating RV variability; and (ii) it provides a combined high-S/N spectrum for stellar parameter determination.

2.2.4 *RV variability*

We determined RV measurements for each spectrum available per target using the co-added spectrum as a baseline. These RVs are calculated using cross correlation[5], based on work by Zucker et al. (2003) and further developed by Shenar et al. (2019) and Dsilva et al. (2020). With at least two spectroscopic epochs for a given star we can calculate a ΔRV (i.e. the maximum absolute variation in RV seen across available spectra). Additional epochs naturally lead to higher precision and better constraints on this value; with only two spectra available we can at least determine a lower limit. From the sample, we identify 277 of the 377 stars with two or more epochs (after removing targets with emission and SB2 systems) as being RV variables. This was assessed by determining whether $\Delta\mathrm{RV} > \sigma\Delta\mathrm{RV}$ (i.e. the maximum variation in RV was larger than its error). This RV variability could result from a variety of processes including pulsation and binarity, but disentangling these effects is difficult with only spectroscopy, especially when only a few epochs are available. This measurement is only utilised for classifying stars in our sample as RV variables, and is separate from the two criteria utilised for determining binarity, as discussed further down in this section.

[4] https://git.io/JqJhf
[5] https://github.com/TomerShenar/Cross-correlation

Following previous spectroscopic studies of massive stars (Sana et al. 2012; Bodensteiner et al. 2021; Banyard et al. 2022; Mahy et al. 2022; Nardini et al. 2025), we apply two RV variability criteria to separate single stars from likely binary systems. We emphasise that identifying binaries from RV variability only yields the observed binary fraction rather than the intrinsic binary fraction, which is obtained by correcting for observational and astrophysical biases (e.g. Sana et al. 2012, 2013).

In our sample of 700 stars (after removing SB2 systems and emission-line stars), only 377 stars have two or more spectroscopic epochs, and only 134 stars have three or more spectroscopic epochs. Therefore, owing to the limited number of epochs, it is not possible to determine orbital periods from the spectra alone. Moreover, for the majority of targets, only a single available epoch means it is impossible to determine any RV variability. As a mentioned previously (c.f. Section 2.2), the RVs for the 377 stars with at least two spectroscopic epochs are determined using their co-added spectra as templates, with weights based on the S/N of the spectra.

The first criterion to identify a candidate binary system is based on whether the RV variability is statistically significant, which is defined as

$$\frac{|v_i - v_j|}{\sqrt{\sigma_i^2 + \sigma_j^2}} > 4.0, \tag{1}$$

where v_i and v_j are two distinct RV measurements, and their corresponding uncertainties σ_i and σ_j, respectively. We adopt an identical threshold for the right-hand side of Eq. 1 as previous studies to limit the impact of false-positives (Sana et al. 2012; Bodensteiner et al. 2021; Banyard et al. 2022; Mahy et al. 2022; Nardini et al. 2025). From the 377 stars with multi-epoch spectroscopy that show RV variability, there are 166 targets that fulfil this criterion.

The purpose of the second criterion is to remove systems with RV variability that may be caused by a physical mechanism other than binarity (e.g. pulsations). To achieve this it is generally assumed that a true binary system has a minimum variation in its RV time series, ΔRV, that is larger than some threshold. The second criterion to identify a binary system is thus

$$\Delta\mathrm{RV} = \left|v_i - v_j\right| > C\ , \tag{2}$$

where C is typically taken as 20 km s^{-1} (Sana et al. 2013; Bodensteiner et al. 2021; Banyard et al. 2022; Mahy et al. 2022; Nardini et al. 2025).

Previous studies have set this threshold at C = 20 km s^{-1} for O-type stars in the Galaxy, LMC and SMC (Sana et al. 2012, 2013, 2025; Simón-Díaz et al. 2024) because such stars do not typically exhibit high-amplitude coherent pulsations. However, exceptions exist, with the massive single star ζ Oph having intrinsic RV variability caused by pulsations exceeding 20 km s^{-1} (Kalita et al. 2025). On the other hand, the choice of this threshold is less clear for B-type stars (see e.g. Villaseñor et al. 2025; Bodensteiner et al. 2025; Britavskiy et al. 2025), especially those in the Milky Way because such stars are commonly pulsators. Banyard et al. (2022) and Nardini et al. (2025) use the same threshold of C = 20 km s^{-1} for different samples of galactic B-type stars in clusters and briefly discuss whether the threshold should be different. This is because the typical RV variability of pulsations in galactic B-type stars can commonly exceed 20 km s^{-1} value (see e.g. Aerts et al. 2009; Simón-Díaz et al. 2024). Moreover, with only a limited set of spectroscopic epochs it is difficult to distinguish pulsations and binarity in galactic B-type stars.

2.2.5 Stellar parameter estimation

Using the co-added spectrum, and the RV shifts determined in the previous step, we also inferred the effective temperature ($T_{\rm eff}$), surface gravity (log g), and projected surface rotational velocity (v sin i), of each star by comparing the co-added spectrum to a grid of synthetic spectra. The procedure follows previous work with similar goals and sample properties (see Bodensteiner et al. 2021). Considering the range of spectral types in our sample, we elected to utilise the TLUSTY grid of models (Hubeny & Lanz 1995; Lanz & Hubeny 2003, 2007). The TLUSTY models are separated into two grids, one for the O-type stars (Lanz & Hubeny 2003) and one for the B-type stars (Lanz & Hubeny 2007), covering the visible wavelength regime (3000-7500 Å) utilised by HERMES. The parameter space of each grid in the visible wavelength regime is shown in Table 1. For our sample of stars, we elected to fix the metallicity to solar ($Z/Z_\odot$ = 1), with microturbulence set to $v_{\rm mic}$ = 2 km s^{-1} for the B-star grid and 10 km s^{-1} for the O-star grid. Additional models were also calculated between 9000 and 15 000 K, in steps of 1000 K, and with surface gravity log g ranging between 3.0 and 5.0 in steps of 0.25 dex, to complement the standard TLUSTY B-star grid and cover the lowest-temperature end of the sample. To account for line broadening due to rotation, the entire grid was convolved using the ROTBROAD[6] package (version 0.22.0), to generate additional models with v sin i values ranging from 0 to 500 km s^{-1} with steps of 20 km s^{-1}. For calculating the stellar parameters, we relied on fitting the synthetic spectra to the Balmer line series, as well as He I lines at 5875, 6678, and 7065 Å, and He II line at 4685 Å. The best-fitting stellar parameters, and their respective errors, were determined using a χ^2 minimisation procedure, as described in Bodensteiner et al. (2023). In short, this is done by comparing the co-added spectrum of a given star to each model in the grid and calculating

$$\chi^2 = \frac{1}{S/N}\sum_{i=1}^{n}(\mathrm{obs}_i - \mathrm{model}_i)^2, \tag{3}$$

where obs$_i$ and model$_i$ are the observed and model spectra respectively at a given wavelength i, with n being the total number of wavelength values tested.

We compared the best-fitting parameters based on the spectra normalised using SUPPNET with those resulting from a manual continuum normalisation for a small subset of stars that span the full O4-B9 spectral range of the sample. We find that the parameter values determined from the two different sets of normalised spectra were within the confidence intervals of each other and are thus consistent. This demonstrates reliability in the automated method via SUPPNET, which proved extremely beneficial for performing this normalisation step on such an extensive sample. Several examples of the comparison between SUPPNET and manual normalisation are shown in Fig. A1 in the Appendix.

2.3 Gaia data

Primarily to verify the stellar parameters we acquired from comparison with the TLUSTY models, we also retrieved effective temperatures, surface gravities, and projected rotational velocities where possible from the *Gaia* DR3 archive (Gaia Collaboration et al. 2023a). We choose the values determined using the Extended Stellar Parametrizer for Hot Stars (ESP-HS; Gaia Collaboration et al.

[6] https://pyastronomy.readthedocs.io/en/latest/pyaslDoc/aslDoc/rotBroad.html

Table 1. Parameter space for the two TLUSTY model grids, including the additionally calculated models, with the grid step size indicated in parentheses for parameters we iterated over.

	B-star	O-star
$T_{\rm eff}$ (K)	9000 – 30 000 (1000)	27 500 – 55 000 (2500)
$\log g$ (dex)	1.75 – 4.75 (0.25)	3.00 – 4.75 (0.25)
$Z/Z_\odot$	0.01 – 2	0 – 2
$v_{\rm mic}$ (km s^{-1})	[2;10]	10
$v \sin i$ (km s^{-1})	0 – 500 (20)	0 – 500 (20)

2023b). The ESP-HS includes corrections to the stellar parameters determined for stars with effective temperatures $T_{\rm eff} \gtrsim 7500$ K, which is the case for our entire sample. Such parameters have been shown to be less reliable when determined using the standard procedures (i.e. the General Stellar Parametrizer from Photometry, GSP-Phot; Fouesneau et al. 2023). The comparisons between the ESP-HS and TLUSTY methods of stellar parameter determinations are discussed in Section 3.2.

2.4 TESS photometric data

In this work, we use time-series photometric data from the NASA TESS space mission (Ricker et al. 2015), which are made publicly available on the Mikulski Archive for Space Telescopes (MAST) at the Space Telescope Science Institute[7].

For the vast majority of the targets in the sample (>96%), 2-min cadence TESS data was available from the MAST database, which formed the basis upon which our photometric analysis was performed. When retrieving data from MAST, the light curves are provided with two different detrending methods, Single Aperture Photometry (SAP) and Pre-search Data Conditioning SAP (PDC-SAP). In almost all cases we relied on the PDC-SAP light curves, which are produced by the NASA SPOC pipeline (Jenkins et al. 2016). Historically these detrended light curves have been shown to generally provide better results for measuring the photometric variability of massive stars (e.g. Burssens et al. 2020; Bowman et al. 2022; Burssens et al. 2023), except sometimes in the case of the brightest stars (e.g. Southworth & Bowman 2022). In our sample, which only had 26 targets with $V < 5$ mag, the PDC-SAP remained the more reliable choice despite testing both methods.

For the portion of the sample for which the 2-min cadence data is not available (25 stars), we instead extracted light curves from the TESS full frame images (FFI), using the Lightkurve (Lightkurve Collaboration et al. 2018) and TESScut (Brasseur et al. 2019) packages to select a 40×40 pixel image around each target from which to extract the light curves. The latter were detrended using a principle component analysis (PCA) method, performed by excluding a 10×10 pixel square centred on the target star and using the remaining pixels in the image as regressors (see e.g. Scott & Bowman 2026).

All the light curves, regardless of their origin, were then subjected to a Fourier analysis to identify significant frequencies associated with one or several variability mechanisms. We calculated frequency spectra using the modified generalised Lomb-Scargle (LS; Lomb 1976; Scargle 1982) periodogram from the Astropy (Astropy Collaboration et al. 2013a, 2018a) package. This not only allowed us to identify the existence of significant peaks that correspond to pulsation mode frequencies, but also to infer the rotation and/or orbital frequencies of stars (see Section 4).

[7] https://archive.stsci.edu/missions-and-data/tess

Generally, we use the same classification criteria as Burssens et al. (2020). For example, stochastic low-frequency (SLF) variability is defined as an excess of power in the low frequency domain not related to coherent modes (Bowman et al. 2019a), slowly pulsating B-type (SPB) stars are main-sequence B-type stars that pulsate in coherent non-radial g modes with frequencies between about 0.2 and 4 d^{-1}, β Cephei (β Cep) stars are main-sequence late O- and early B-type stars that have low-radial order p- and g-mode frequencies between about 2 and 25 d^{-1} (see Bowman 2020). However, we note that it is difficult to distinguish all the potential variability mechanisms operating in a massive star from its light curve alone. When classifying all stars based on their TESS light curves and corresponding frequency spectra, we note that frequencies below about 0.5 d^{-1} could be instrumental (e.g. imperfect detrending) or astrophysical (e.g. rotational modulation).

Each sector of available TESS data for a star is considered individually to check for the existence and consistency of variability seen across all its light curves. This is useful for a number of reasons; for example, to distinguish between SPB pulsation modes and SLF variability in the low frequency regime, as the g modes in an SPB star are typically coherent and should be generally consistent across sectors, whereas SLF variability is non-periodic. Some stars presented a combination of these features, in which cases all types of variability were taken note of. For classification purposes, priority is given to the dominant type of variability that is consistently observed across all sectors of available TESS data.

3 ENSEMBLE RESULTS

Of the 873 stars included in our sample, based on our analysis of TESS mission data we have classified based on frequency analysis 197 stars with g-mode pulsations characteristic of SPB stars, 251 stars with p- and/or g modes typical of β Cep stars, and 268 stars showing SLF variability (see Section 4). This represents a pulsator fraction of over 80 per cent, which is consistent with previous studies (Bowman et al. 2019a; Burssens et al. 2020). We also identify 67 eclipsing binaries (EBs), 30 of which were not previously known in the literature. The TESS light curves have also yielded 148 stars to show rotational modulation (sec Section 6). From analysis of the available HERMES spectra, we identify 353 of the 873 stars to have RV variability (or 76 per cent of the 464 stars with at least 2 spectra), with 51 of these satisfying the two statistical criteria for binarity (see Section 5). Finally, we also identify 19 SB2 systems, 127 OBe stars, and 26 blue supergiants (BSGs), all of which we do not investigate further in this study and leave for future work since such systems require dedicated individual analysis. The full breakdown of all our classifications is provided in Table 2.

3.1 Spectroscopic Hertzsprung–Russell (HR) diagram

Once satisfied with the visual classification and corresponding stellar parameter determination, we generated the spectroscopic HR diagrams shown in Fig. 2, in which the spectroscopic luminosity values are defined as $\mathcal{L} = T_{\rm eff}^4/g$ following Langer & Kudritzki (2014), for the 322 stars with available parameters from *Gaia* ESP-HS database. We note that only 37 per cent of our sample have such parameters.

We choose to use the *Gaia* ESP-HS parameters, instead of the TLUSTY-derived parameters purely when plotting an HR diagram, because the discrete sampling of the TLUSTY grid does not yield as informative a visual distributions in the HR diagram. For the remainder of this article, however, we rely exclusively on the $T_{\rm eff}$, $\log g$,

Table 2. The different variability types classified in our sample, which have been divided into subgroups of O- and B-type populations based on their SIMBAD spectral type. Column 4 denotes the number of stars that fulfil both binarity criteria from our RV calculations making them candidate spectroscopic binaries, column 5 denotes the number of SB2 systems, column 6 denotes the number of stars known in the SBX catalogue (Pourbaix et al. 2004; Merle et al. 2026), and the numbers of EBs are given in column 7, with the parentheses denoting those that were previously known in the literature. The full table of stellar parameters and classifications are available in the supplementary material.

	Luminosity class		Binarity				Pulsation			Other			
SpT	Giant	Dwarf	RV criteria	SB2	SBX catalogue	EB	SPB	β Cep	SLF	RotMod	OBe	BSG	Total
O	28	33	2	2	2	4 (0)	0	7	48	5	9	4	61
B	471	341	49	17	26	63 (37)	197	244	220	143	119	22	812

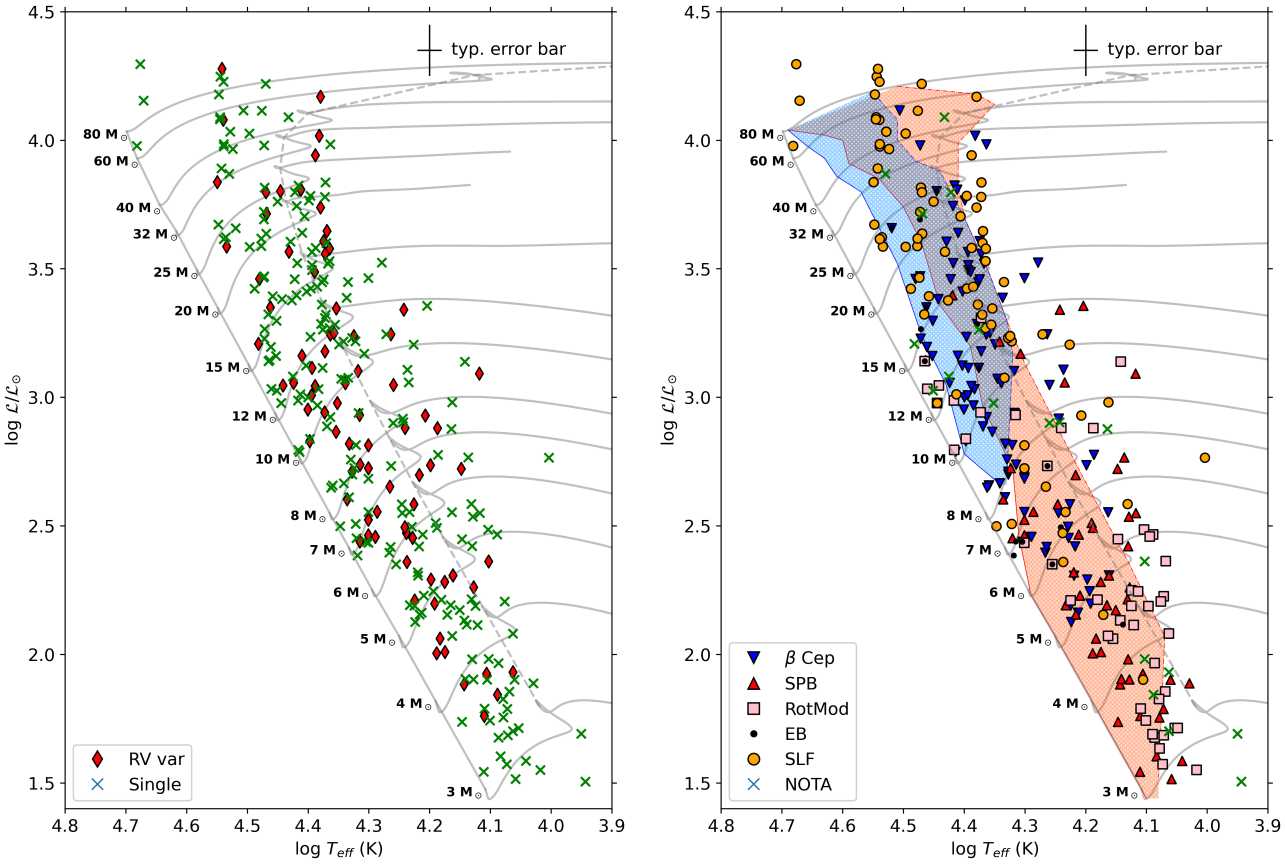

Figure 2. Spectroscopic HR diagrams for the 322 stars in our sample with available stellar parameters from the *Gaia* ESP-HS database, which show our classifications based on HERMES spectroscopy (left) and TESS photometry (right). For both cases, we use the evolutionary tracks for a range of masses (solid grey lines) from Burssens et al. (2020). The zero-age main sequence (ZAMS) and terminal-age main sequence (TAMS) are denoted by solid and dashed grey lines, respectively. For the photometric case in the right panel, the theoretical instability strips corresponding to p-mode (blue) and g-mode pulsations (red) from Burssens et al. (2020) are also shown. Stars not presenting any of the other features shown in the respective legends are labelled as 'NOTA' (None Of The Above).

and v sin i parameters we determine from synthetic spectrum fitting using the TLUSTY grids. In the left panel of Fig. 2 we have denoted the subsamples of stars with significant RV variability, compared to the population without.

In Fig. 2, we also include non-rotating evolutionary tracks calculated by Burssens et al. (2020) with the MESA stellar structure and evolution software package (Paxton et al. 2011, 2013, 2015, 2018, 2019). The evolutionary tracks are for solar metallicity ($Z_{\rm ini}$ = 0.014), a heavy element mixture appropriate for massive stars from Nieva & Przybilla (2012), OP opacity tables (Paxton et al. 2011), a scaled mass-loss rate with a factor of 0.5 compared to Vink et al. (2001), an exponential diffusive convective boundary mixing (CBM) prescription of $f_{\rm CBM}$ = 0.02, and a constant minimum envelope mixing value of $\log D_{\rm env}$ = 1.0 (Burssens et al. 2020). The evolutionary tracks cover birth masses between 3 and 80 $M_\odot$, which is sufficient to cover our sample, and are calculated from the zero-age main sequence (ZAMS) up to near-depletion of core hydrogen mass fraction. In addition, from these models we define the terminal-age main-sequence (TAMS) as the point in the models where $X_c < 10^{-5}$. We emphasize, however, that the evolutionary tracks shown do not include binarity, magnetism, are non-rotating, and only include a single prescription for envelope and convective boundary mixing (CBM), all of which are known to play important roles in stellar evolution (e.g. Ekström et al. 2012; Aerts et al. 2019; Temaj et al. 2024).

In the right panel of Fig. 2, we show the same sample but with symbols that denote the dominant photometric variability as determined

by our analysis of the TESS light curves and corresponding frequency spectra. These include β Cep stars, SPB stars, stars with rotational modulation (RotMod), eclipsing binaries (EB), stars with stochastic low-frequency (SLF) variability (see Bowman et al. 2019b), and any stars showing none of the above (i.e. NOTA). In addition, we have also included the theoretical pulsation instability regions calculated by Burssens et al. (2020) by solving the non-adiabatic stellar pulsations equations using GYRE (Townsend & Teitler 2013; Townsend et al. 2018). The two instability regions denote where one expects to find low-radial order p modes (blue; $1 \leq n \leq 5$), and a mix of low- and high-radial order g modes (red; $-50 \leq n \leq -1$), for angular degrees of $0 \leq \ell \leq 2$ and $1 \leq \ell \leq 2$ for p modes and g modes, respectively. The hotter boundaries of the p- and g-mode instability regions are denoted by solid lines in Fig. 2, whereas the cooler boundaries are denoted by dashed lines. The GYRE calculations of Burssens et al. (2020) only calculated instability regions for main-sequence MESA models, and therefore did not include the post-main sequence phase of stellar evolution.

We emphasize that any calculated instability region is only applicable to the specific evolutionary tracks used as input. This means that any difference in rotation rate, interior mixing, or mass loss rate, which inevitably changes the evolutionary tracks, would also change the location of the instability regions. Moreover, rotation not only changes the amount of mixing inside a star, but also influences the eigenfrequencies and the balance of driving and damping processes of pulsations (see discussions by Townsend 2005; Szewczuk & Daszyńska-Daszkiewicz 2017). Therefore, the evolution of stars, and whether they are expected to pulsate or not, within the mass regime discussed in this study are very sensitive to the choice of input parameters, such that small changes in parameter combinations can have large impact on the location of both the evolutionary tracks and the corresponding instability regions (see also Paxton et al. 2015). This means we consider the evolutionary tracks in Fig. 2 to be representative, but not perfect. Similarly, the instability region calculations only include a single excitation mechanism and are therefore not expected to give a complete image of where we can expect pulsations (see, e.g. Hey & Aerts 2024).

3.2 Comparing parameters derived from TLUSTY and *Gaia*

In Fig. 3, we compare the atmospheric parameters deduced from our grid-based fitting of TLUSTY models with those available from the the *Gaia* ESP-HS database. Upon first inspection, while the two sets of $T_{\rm eff}$ values appear to be largely consistent, there are a subset of stars which have fairly large differences. The (dis)agreements in Fig. 3 are somewhat worse for $\log\ g$ and $v\ \sin\ i$, and can be understood because of a number of factors, which we discuss below.

Firstly, Fouesneau et al. (2023) suggests that $T_{\rm eff}$ values determined from ESP-HS tend to be underestimated by about 2000 K for stars with $T_{\rm eff} \gtrsim 25\,000$ K when compared to large spectroscopic surveys, such as DR6 of the Large Sky Area Multi-Object Fibre Spectroscopic Telescope (LAMOST; Zhao et al. 2012; Cui et al. 2012; Xiang et al. 2022). This is somewhat visible in the left panel of Fig. 3, where we see a slight bias of points above the unity line, further accentuated by the linear regression to the data points (red dashed line) becoming increasingly offset beyond about ~25 000 K. While this offset does not appear to be systematically equivalent to 2000 K, the fit suggests that the offset deteriorates towards increasingly higher values of $T_{\rm eff}$.

Secondly, *Gaia* $\log\ g$ values calculated by the astrophysical parameters inference system (Apsis; Bailer-Jones et al. 2013) are determined primarily through fitting a grid of synthetic spectra in BP/RP photometry and low-resolution RVS spectra (when available) using a χ^2 minimisation, using the Balmer and Paschen lines as anchors. These spectral lines reach a maximal strength at $T_{\rm eff} \simeq 8500$ K and, above this threshold, there is a noticeable underestimation of $\log\ g$ in the GSP-Phot values. This offset is somewhat corrected for in ESP-HS by using a grid of synthetic spectra tailored to hot stars and by focusing on the Balmer line series and helium lines for surface gravity determination. For example, an improvement in accuracy by a factor of two with respect to GSP-Phot is expected for the magnitude range of our sample (Fouesneau et al. 2023; Gaia Collaboration et al. 2023b). That said, a systematic scatter of about 0.2 to 0.4 dex is expected for the derived $\log\ g$ values from *Gaia* ESP-HS, particularly when extending to the higher temperature ranges ($\gtrsim$ 30 000K). This scatter is seen when comparing the *Gaia* ESP-HS values to our grid-based TLUSTY fitting values in the middle panel of Fig. 3. We emphasize that the step size of $\log\ g$ in the TLUSTY grid is larger than that of *Gaia* in a relative sense, which produces 'rows' of values to stack on top of each other in the middle panel of Fig. 3.

Finally, to measure $v\ \sin\ i$ in ESP-HS, *Gaia* assumes that effectively almost all spectral line broadening is due to rotation, by convolving and fitting the full synthetic spectra with rotational broadening kernels (Fouesneau et al. 2023), which is not provided at all by the standard GSP parametrisation. While this is a reasonable approximation for low- and intermediate-mass stars (see Gray 2005), the spectral lines of massive stars have considerable additional broadening mechanisms. For example, microturbulence and macroturbulence both have a significant impact on the shape of spectral lines (see Aerts et al. 2009; Simón-Díaz et al. 2017; Kalita et al. 2025). By default, *Gaia* assumes a standard value of $v_{\rm mic} = 2$ km s^{-1} for microturbulence, which aligns with the available value in the B-star grid of TLUSTY models we used in this work, though differs to the 10 km s^{-1} value utilised for the O-star TLUSTY grid. Neither *Gaia* nor the TLUSTY models include macroturbulence as an additional fitting parameter, and are therefore not considered as a source of line broadening. Another factor could be that of additional SB2 systems that went unnoticed in our spectroscopic analysis, where blended lines might appear as one star in certain epochs and as two stars in another, resulting in an overestimation of the width of the given line in one instance or the other. We nonetheless observe that the majority of points (and in particular almost all of the outliers) fall below the unity line in the right panel of Fig. 3, indicating that *Gaia* almost systematically overestimates the $v\ \sin\ i$ values with respect to those we calculated using the TLUSTY models.

Therefore, we conclude that *G*aia ESP-HS produces reliable $T_{\rm eff}$ values, on average, for massive stars, which are useful for ensemble analysis. However, high-resolution spectroscopy is highly beneficial when studying $\log\ g$ and $v\ \sin\ i$ for massive stars, especially for those in binary systems (see Section 5).

3.3 Population of evolved stars

A minority of the stars in our sample appear to have evolved beyond the TAMS according to the evolutionary tracks calculated by Burssens et al. (2020) and parameters determined from *Gaia* ESP-HS, shown in Fig. 2. This conclusion is based on evolutionary tracks that include only a modest amount of CBM, with the diffusive exponential prescription of $f_{\rm CBM} = 0.02$. Massive stars are expected to evolve rapidly across the Hertzsprung gap after the main sequence, so it may seem surprising to observe a significant portion of the sample located in this region of the HR diagram. However, we note that the main-sequence lifetime of a massive star and thus the position of the TAMS are highly sensitive to the input parameters, for example rotation, mixing, and metallicity, used in the evolution tracks shown in

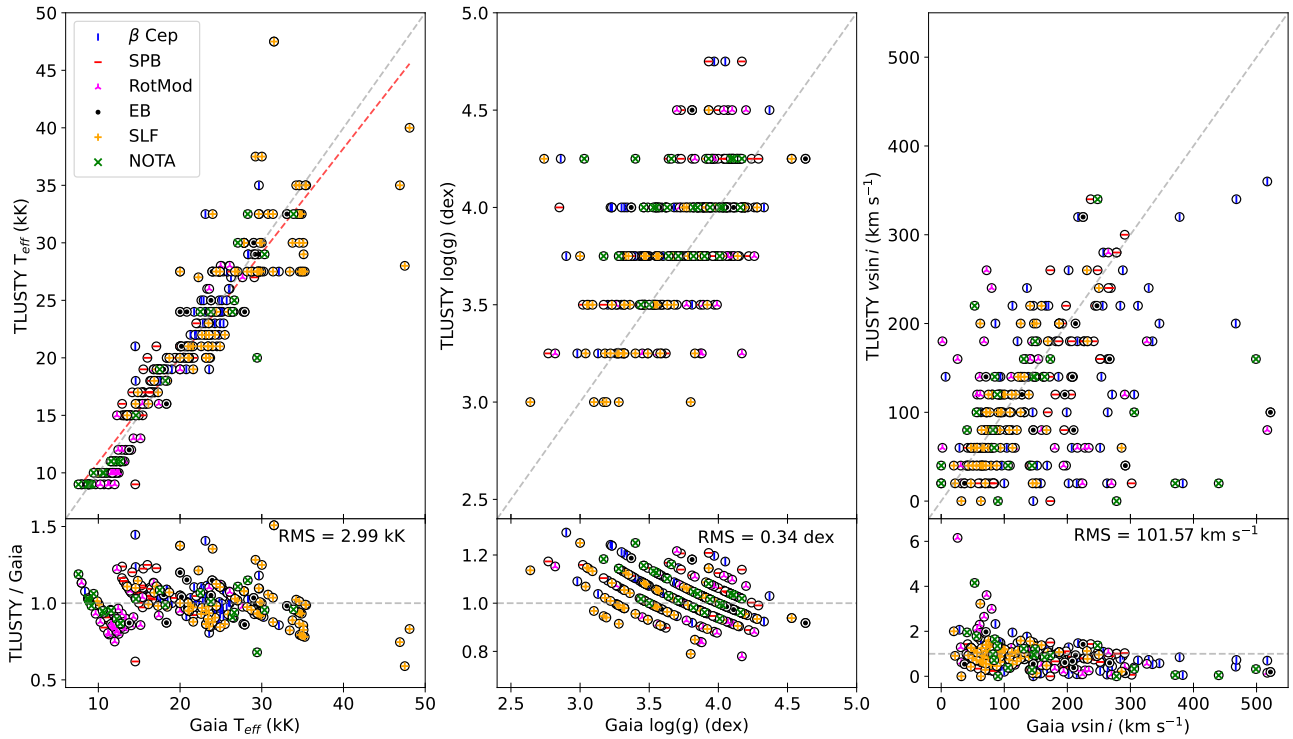

Figure 3. Comparisons of stellar parameters from the *Gaia* ESP-HS database to those determined in this study using a grid-based fitting of TLUSTY atmospheric models. Targets have been labelled with respect to their photometric classification. Grey dashed lines corresponding to unity have been drawn for clarity, and an additional red-dashed line has been added for the $T_{\rm eff}$ plot, representing a linear regression to the data points (see Section 3.2). The bottom row corresponds to the TLUSTY/*Gaia* residuals for each parameter, and the resulting RMS values.

Fig. 2 (see Bowman 2020; de Burgos et al. 2025; Martins & Palacios 2013; Ekström et al. 2012; Gilkis et al. 2021; Castro et al. 2014). As such, stars seemingly redder than the TAMS may still be main-sequence stars with large amounts of interior mixing, or undergoing blue loops, or the results of merger products, etc.

4 PULSATING STARS

Similar to the previous study of massive stars in the Southern hemisphere by Burssens et al. (2020), we find a high pulsator fraction (> 80 per cent) for galactic massive stars. Typical examples of the TESS light curves and corresponding frequency spectra from the coherent pulsator classes of β Cep and SPB stars are shown in Fig. 4. Within the sample, there exist many coherent pulsators that offer excellent prospects for forward asteroseismic modelling (e.g. Pedersen et al. 2021; Burssens et al. 2023), which is the subject of future work (Scott et al. in prep).

4.1 Pulsation instability regions

As shown in the right panel of Fig. 2, we find that the majority of the β Cep and SPB pulsators in our sample lie within their respective instability regions in the HR diagram. On the other hand, there is a small subset of evolved β Cep stars located cooler than the TAMS as calculated in the evolutionary tracks by Burssens et al. (2020). As mentioned previously, these evolutionary tracks are non-rotating and only assume a single set of physical assumptions, such that a larger amount of mixing would prolong a star's main-sequence lifetime, and hence displace the TAMS to cooler temperatures. Although the number of post-main sequence β Cep stars is low in the literature, with some even being explicitly referred to as near the TAMS (e.g. V453 Cyg A; Pavlovski & Southworth 2009; Southworth et al. 2020), the number of β Cep stars beyond the model grid TAMS observed in our sample only represent a small fraction of the full sample. They could potentially be explained by varying the input physics of our evolutionary tracks (i.e. mixing parameters or binary effects) to extend the main sequence to cooler effective temperatures to encapsulate all the observed β Cep stars.

In the HR diagram in Fig. 5, we show density contours that are defined as large fractions of stars showing a common type of pulsation. Therefore, these contours represent the empirical instability regions for each of the three main pulsator types: β Cep, SPB, and SLF variability. Specifically, the hatched contours represent the region containing 66 per cent of each pulsator population, and the filled contour represents the 33rd percentile of the observed population for each pulsator type.

For the β Cep stars, the sample of 119 stars from Fritzewski et al. (2025) follow a similar distribution to those in our sample. However, while noting the difference between bolometric and spectroscopic luminosity, our sample is shifted towards lower masses, with at least 66 per cent of the population being contained within the 5 to 20 $M_\odot$ range (with a few outliers up to 60 $M_\odot$ seen in Fig. 2), compared to their range of reported evolutionary masses: 6.5 – 32 $M_\odot$. A similar comparison of the location of the empirical SPB instability region is performed with the observed population of 52 SPB stars from Pedersen (2022), which range from 3 – 8 $M_\odot$. Our sample of SPB stars is mostly in agreement, with at least 66 per cent of the population covering the same evolutionary mass range. Interestingly, despite the

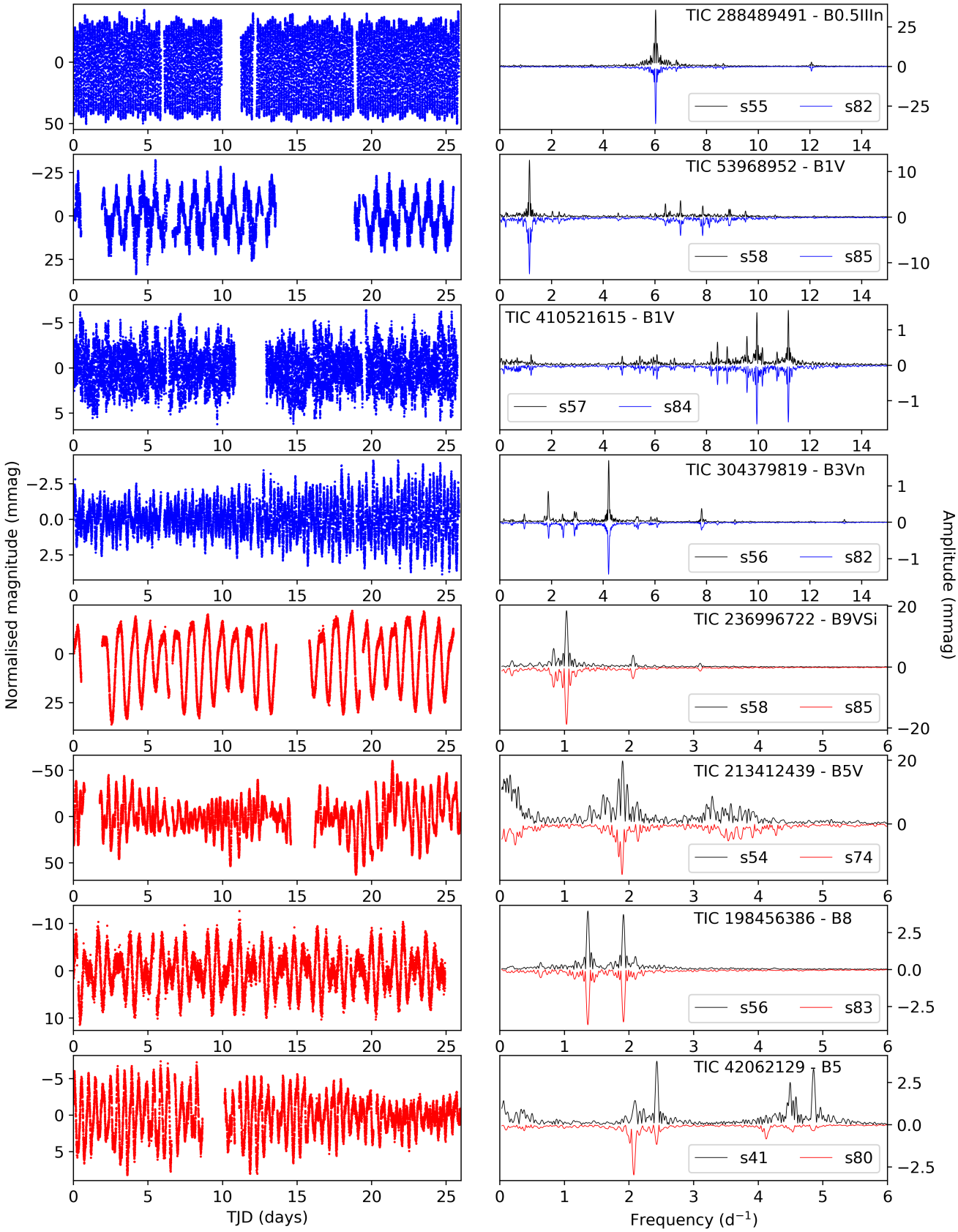

Figure 4. TESS light curves and Lomb-Scargle (LS) periodograms for four β Cep (blue; TIC 288489491, TIC 53968952, TIC 410521615 and TIC 304379819) and four SPB stars (red; TIC 236996722, TIC 213412439, TIC 198456386 and TIC 42062129). The LS periodograms show two different sectors in blue (red) and black for comparison purposes, whereas the light curves show only the TESS sector correspondingly coloured in the blue (red) periodograms.

number of excited g modes in SPB stars being generally larger for masses of about 3-4 $M_\odot$ (see figure 11 of Pedersen et al. 2020), the mass range in which the highest fraction of SPB stars is found in our sample is between 4-6 $M_\odot$. We postulate that this in predominately an impact of metallicity, for example, the difference between OP and OPAL opacity tables used by us and Pedersen et al. (2020) respectively (see Paxton et al. 2015 and Moravveji 2016). Finally, Bowman et al. (2020) find that majority of main-sequence stars with SLF variability as their dominant variability type are O-type stars, which is in agreement with our sample.

More generally, the two coherent pulsator types, β Cep and SPB stars, are found across the whole main sequence in Fig. 5, which contains evolutionary tracks with an assumed amount of CBM being $f_{\rm CBM} = 0.02$ (Burssens et al. 2020). This lends support to the idea that this amount of CBM is reasonable for a population study of main-sequence stars with masses between about 3 and 15 $M_\odot$. However, the population of stars with SLF variability are mostly found towards the latter half of the main sequence and are generally found near the TAMS. For masses above ~15 $M_\odot$, assuming all stars with SLF variability are main-sequence stars in our study, a larger amount of CBM than $f_{\rm CBM} = 0.02$ (or the inclusion of rapid rotation in the models) would be needed to shift the TAMS to cooler temperatures and encapsulate these stars as main-sequence stars. This is, of course, heavily dependent on the various parameters that dictate the location of the TAMS, as described in Sec. 3.1.

There exists a subset of β Cep stars in our sample with masses between 5–7 $M_\odot$, determined by their position in the HR diagram, which is atypically low mass for such stars (supported by the findings of Fritzewski et al. 2025). These stars are approaching the regime where we might expect to find δ Scuti stars, which also present high-frequency pulsation peaks (between $\sim 5 - 50$ d^{-1}), though in these stars it is due to the He II opacity bump as opposed to the metal opacity bump in the case of β Cep stars. Indeed, particularly in the case of strong magnetism, it has been found that the δ Scuti instability strip can be extended to higher temperatures and luminosities (Thomson-Paressant et al. 2025). Distinguishing these two populations would require additional photometric follow-up and investigation, using asteroseismic modelling to determine the nature of the excitation mechanism.

Finally, we note that there is significant overlap among the three different pulsator types in Fig. 5. This is not unexpected since so-called 'hybrid' pulsators of β Cep and SPB stars have been known for some time (see Handler 2009). Moreover, many stars show multiple distinct variability types in our sample; for example, both high-frequency p modes typical of β Cep stars as well as SLF variability. In this exercise, however, we have only labelled the dominant variability type of each star, which means that hybrid stars are not a distinct pulsator type.

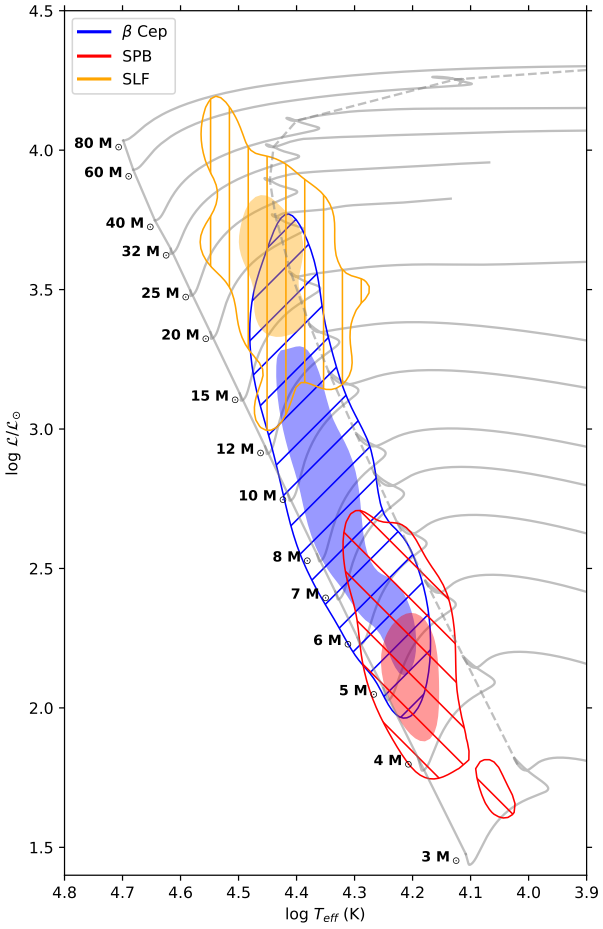

Figure 5. Spectroscopic HR diagram showing the distribution density of the three main pulsator types found in the sample (β Cep, SPB, and SLF). Contours are drawn at the 66th and 33rd percentiles in terms of population intervals for the hatched and filled regions, respectively.

4.2 SLF variability

The dominant physical cause of SLF variability in massive stars remains debated in the literature, and may even arise from a combination of different physical mechanisms that dominate in different parts of the HR diagram (see Bowman 2023). One proposed mechanism is internal gravity waves (IGWs) excited at the turbulent convective core boundary (Rogers et al. 2013; Rogers & McElwaine 2017; Edelmann et al. 2019; Anders et al. 2023; Thompson et al. 2024; Pathak et al. 2025), which propagate to the stellar surface and produce a broad, low-frequency power excess in photometry (Blomme et al. 2011; Aerts & Rogers 2015; Bowman et al. 2019a, 2020). Another contribution to SLF variability can come from the consequences of sub-surface convection zones which are associated with opacity bumps, typically corresponding with the H, He or Fe ionisation regions/opacity peaks. These zones can excite IGWs or induce turbulence that manifests as SLF variability (Cantiello et al. 2021; Schultz et al. 2022). A third mechanism is variability in the radiatively driven winds of massive stars, for which stochastic changes in wind density, clumping, or large-scale structures introduce low-frequency brightness fluctuations, which is particularly important for the most luminous and evolved massive stars (Krtička & Feldmeier 2018, 2021). The relative importance of these mechanisms is expected to depend on stellar mass, evolutionary state, and wind strength.

SLF variability has emerged as a ubiquitous phenomenon in massive stars with the advent of high-precision space photometry (Bowman et al. 2019a). The morphology of SLF variability correlates with mass and evolutionary state, demonstrating a direct link between SLF variability and a star's internal stellar structure (Bowman et al. 2020; Bowman & Dorn-Wallenstein 2022; Pedersen & Bildsten 2025). More recent studies have shown that the observed SLF properties are largely insensitive to metallicity (Bowman et al. 2024, Van Daele et al., submitted to MNRAS), which supports the interpretation that the dominant driving mechanism is likely not dominated by

instabilities that depend directly on opacity (e.g. sub-surface convection).

Whilst remaining agnostic on the cause(s) of SLF variability in our sample of massive stars, we find it to be ubiquitous in stars with masses above about $M \gtrsim 12$ M$_\odot$, with a handful of suggested cases appearing in masses as low as 4 M$_\odot$, and it is generally the dominant form of photometric variability in stars above about $M \gtrsim 15$ $M_\odot$, as shown in Fig. 5. This is in agreement with previous studies of galactic massive stars (Bowman et al. 2019a,b, 2020). In a future study, we shall investigate the sub-sample of stars with SLF variability in detail (Van Daele et al., in prep.).

4.3 Pulsations and rotation

The distributions of v sin i values we derived from grid-based fitting of rotationally broadened TLUSTY atmospheric models for each of the three main pulsator types are shown in Fig. 6. About half of the 664 pulsating stars are identified as slow-to-moderate rotators based on their projected surface rotational velocities. For example, 301 of the 664 pulsators have v sin $i \leq 100$ km s^{-1}, and a further 134 stars have $100 < v$ sin $i \leq 200$ km s^{-1}. Additionally, 74 stars have v sin $i \leq 30$ km s^{-1}, which may constitute a sample of very slow rotators. These distributions are consistent with the results of previous ensemble studies (e.g. Simón-Díaz & Herrero 2014; Simón-Díaz et al. 2017; Burssens et al. 2020). The few examples with values v sin $i > 300$ km s^{-1} have all been assessed manually to verify the goodness-of-fit of the TLUSTY model from which the parameter determination was performed, and are confirmed to be reasonable. As a reminder, we have omitted the OBe stars from our sample, so the presence of rapidly rotating stars without emission is interesting to follow up. For example, such rapidly rotating stars may be the products of binary interaction (see, e.g. de Mink et al. 2013) or OBe stars in quiescent periods.

The 200 β Cep stars show a large range of v sin i values, with the majority being slow-to-moderate rotators ($0 < v$ sin $i \leq 150$ km s^{-1}). However, a fast rotating tail of the distribution reaches an upper value of about 300 km s^{-1}. The average rotation rate is 95 km s^{-1}. This is consistent with the findings of Stankov & Handler (2005), who suggest that this might be due to a selection effect, as slower rotating β Cep stars show the highest amplitude and most easily identified as pulsators. However, we note that the ensemble study of Stankov & Handler (2005) is based on ground-based detections of β Cep stars, which have a typical photometric precision of order 1 mmag. Whereas space photometry, such as the TESS light curves we have used in the current study, have a typical photometric precision of about 10 μmag. Therefore, our modern sample of β Cep stars should be less biased towards finding faster rotators than Stankov & Handler (2005), and yet we find similar results. Therefore, it is reasonable to conclude that β Cep stars are generally slow-to-moderate in their surface rotation rates.

We see a similar distribution of v sin i values in the SPB stars to the β Cep stars, though the range extends to slightly larger values of 350 km s^{-1}. The average rotation rate of the 116 SPB stars in our sample is 116 km s^{-1}. Finally, for the 167 stars with dominant SLF variability, the v sin i values are typically lower with the gross majority smaller than 150 km s^{-1}, with an average value of 89 km s^{-1}.

5 BINARITY

To assess the fraction of our sample that are in multiple star systems, it is important to separate the binaries from other types of variability

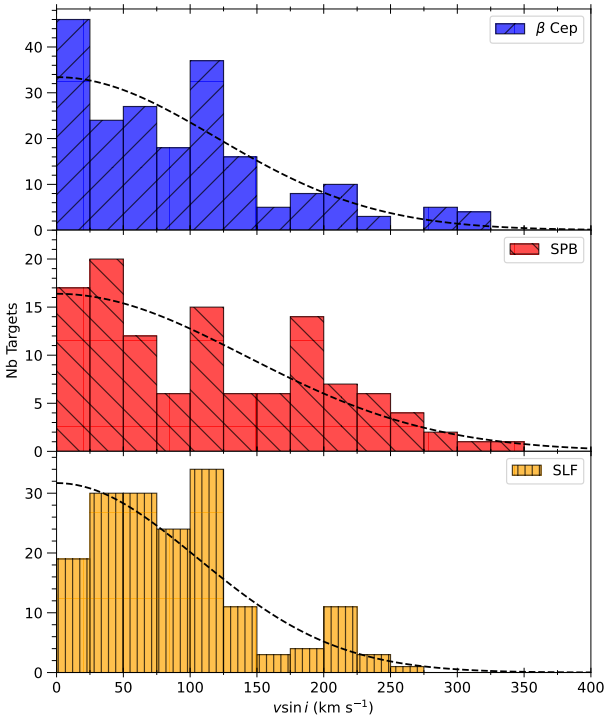

Figure 6. Distributions of v sin i values derived in this work from grid-based fitting of rotationally broadened TLUSTY atmospheric models for the three main pulsator types: 200 β Cep stars, 116 SPB stars, and 167 stars with SLF variability as their dominant type of photometric variability. A normal distribution fit centred on 0 km s^{-1} (black dashed line) has been overplot for each subset.

that may mimic the signatures of binarity (e.g. pulsation, rotational modulation; IJspeert et al. 2021; Prša et al. 2022). The combination of spectroscopic and photometric data has revealed a variety of different types of binary systems within our sample, including many that also pulsate.

5.1 Eclipsing binaries

From the analysis of the TESS photometry, we identify 67 eclipsing binaries. This includes 37 that have already been identified in the literature from previous surveys (e.g. Malkov et al. 2006; Avvakumova et al. 2013; IJspeert et al. 2021; Prša et al. 2022; Mowlavi et al. 2023; Eze & Handler 2024). Therefore, we add 30 new eclipsing binaries in this work. Light curves for those with 2-min cadence TESS data are visible in Figs. B1-B5, along with orbital period estimates. Of these 30, a half (16) have orbital periods shorter than 3 d. A few targets (e.g. TIC 106781544) have large and unconstrained orbital periods ($P_{\rm orb} \gtrsim 13.5$ d) because only a single eclipse is visible in a single TESS sector, thus making accurate period determination impossible. Unless those targets also had back-to-back sectors that contained at least one eclipse each, we could only determine a lower threshold for their orbital period.

We additionally find that 12 of the full list of 67 eclipsing binaries have β Cep or SPB pulsations, as well as a further 11 systems with SLF variability. Both TIC 91111448 (Chen et al. 2022) and TIC 434723918 (Southworth & Bowman 2022) were previously known in the literature as pulsating (β Cep) eclipsing systems (see also Eze & Handler 2024). Six of these EBs are also identified as SB2s in our spectroscopic analysis, which are particularly powerful

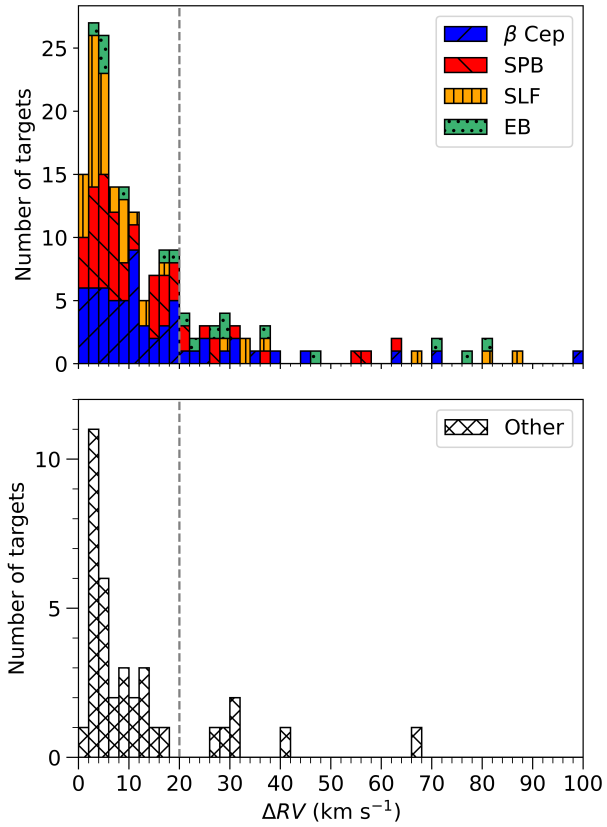

Figure 7. Top panel: Stacked distributions of the calculated ΔRV values for the three main types of pulsating star in the sample, in comparison to the EB population. Bottom panel: ΔRV value distribution for all targets in the sample that are not identified as a pulsator nor an EB from their TESS light curve. In both panels, the grey dashed line corresponds to the commonly adopted threshold for binarity of $C = 20$ km s^{-1}.

laboratories for constraining stellar structure and evolution theory (see Southworth & Bowman 2025). We leave the detailed analysis of the new (pulsating) EBs discovered in this work for a future study.

5.2 Spectroscopic binaries

Our sample contains a grand total of 124 binary systems, which includes 19 targets classified as SB2, 28 targets included in the SBX binarity catalogue (Pourbaix et al. 2004; Merle et al. 2026), 67 EB systems (of which 10 fulfil both binarity criteria), and 51 targets that fulfil both RV variability criteria described above (assuming $C = 20$ km s^{-1}). Considering exclusively binaries detected through our analysis of the HERMES spectra results in a total of 82 systems. Both of these values are modest fractions of the 873 stars in the full sample (124/873 = 14 per cent) and 377 stars with two or more spectroscopic epochs (82/377 = 22 per cent, excluding emission-line stars and SB2), respectively, and are much lower than previous studies (Sana et al. 2012; Bodensteiner et al. 2021; Banyard et al. 2022; Mahy et al. 2022; Nardini et al. 2025; Frost et al. 2025), who generally find observed binary fractions of order 50 per cent or higher from dedicated spectroscopic campaigns. Indeed, with additional spectroscopic epochs, it becomes more likely to detect RV variability and identify binary systems, so our observed binary fraction is a lower limit.

In Fig. 7, we show the ΔRV distribution for the subset of pulsators that fulfil only the first binary detection criterion (cf. Eqn. 1), with a dashed grey line demonstrating the classically adopted $C = 20$ km s^{-1} threshold for the second criterion (cf. Eqn. 2). Also in Fig. 7, we have included the photometric classification of the stars based on the TESS light curves (see also Fig. 2) to gain a perspective on the relationship between RV variability and the different pulsator types. Clearly, all three types of pulsator exist above and below the threshold of 20 km s^{-1}, which makes the value of C in Eqn. (2) a somewhat ambiguous choice. We have also included in Fig. 7 18 EBs from our sample that satisfied the first binarity criterion (i.e. $\Delta RV > 4.0$), of which 12 have at least three spectra, to demonstrate that such systems also exist above and below the 20 km s^{-1} threshold.

Importantly, there are a number of pulsating stars with very large ΔRV values. Examples include TIC 53968952 and TIC 288489491, whose light curves and LS periodograms are shown in Fig. 4, which have ΔRV values of 44.5 and 20.5 km s^{-1}, respectively. Without photometric data, such systems would likely be labelled as binaries by default since their RV variability passed both binary detection criteria. Yet, their photometric variability is also quite large (43 and 93 mmag, respectively) and as such would be sufficient to cause large RV variability. Therefore, we advocate that spectroscopic binary studies of massive stars, and especially galactic B-type stars, should be complemented with photometric data to confirm or refute the presence of large-amplitude pulsations.

5.3 Discussion

5.3.1 Binary fraction

In this work, based on a sample of 377 O- and B-type stars with two or more spectroscopic epochs (and no emission or SB2 features), about 22 per cent of the stars have significant RV variability that passed both binary threshold criteria. However, the majority of these systems are also pulsating stars and their significant RV variability could be caused by pulsations. After having removed the pulsators identified using TESS light curves, the RV distribution for the sub-sample of non-pulsating binary candidates is shown in the bottom panel of Fig. 7. For comparison, the distribution for the pulsating stars with significant RV variability is shown in the top panel. Therefore, the number of non-pulsating binaries that satisfy both criteria is 1 per cent of the full sample. However, we emphasise that this is likely an underestimate of the true binary fraction because of different observational and astrophysical biases, which are discussed below.

First, we have excluded pulsators from the distribution in the bottom panel of Fig. 7, but it is important to note that galactic B-type stars are commonly both pulsators and found in binary systems (Burssens et al. 2020; Southworth & Bowman 2022; Eze & Handler 2024). However, the limited number of spectroscopic epochs for our sample means it is not possible to confidently identify if the significant RV variability arises from pulsations, binarity, or both. In our investigation, we have chosen to be conservative and assume that if a star is found to be a pulsator based on its TESS light curve then the spectroscopic RV variability could be caused by pulsations, which means it may not be a binary. Of course, this may be incorrect, since most stars may in fact be pulsating binaries and spectroscopy alone is difficult to establish this. In the ideal scenario, one should check if the candidate binary period found in spectroscopy matches a pulsation period identified in photometry taking all available information into account, such as range of expected pulsation periods given the star's location in the HR diagram. For example, if a star has a significant spectroscopic binary period larger than about 20 d, then this is too large to be a heat-driven pulsation period in a main-sequence β Cep

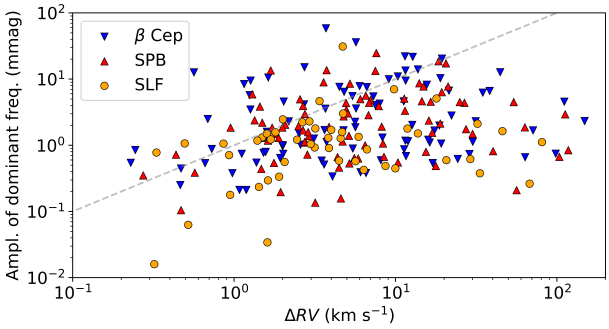

Figure 8. Comparison between calculated ΔRV values measured from multi-epoch HERMES spectra versus the amplitude of the dominant pulsation frequency based on TESS data, which are divided into the three main pulsator types. The dashed grey line is simply a unity line (i.e. not a fit) between the axis quantities (1 km s^{-1} = 1 mmag).

star. On the other hand, if the identified spectroscopic period is of order a few days and similar periods are found in photometry indicating pulsations, this is a strong indication that the spectroscopic period is a pulsation period for such a star. Indeed, spectroscopic identification of pulsation periods, especially in B-type main-sequence stars, is a powerful technique for pulsation mode identification (see Aerts et al. 2010).

Second, with only a few spectroscopic epochs, we are not sensitive to all possible binary orbital configurations. The selection function depends on the cadence and total time span of the observations, which is star dependent in our case and far from uniform across the sample. With an average cadence of the order of a month, and only two or three epochs, it is entirely possible to have missed a large range of orbital periods. Regardless, all systems with significant RV variability identified in this work are worthy of continued monitoring with spectroscopy to ascertain their binary status and the relationship to pulsations. Indeed, the interaction of binarity and pulsations — tidal asteroseismology — is an emerging field and very powerful for probing the physics of binary star evolution (see Southworth & Bowman 2025).

5.3.2 *Choice of the 20 km s^{-1} threshold*

On first inspection, the 20 km s^{-1} threshold in the second of the binary criteria (c.f. Eqn. 2) appears to align well with the overall ΔRV distribution for pulsating and non-pulsating stars in Fig. 7, since we find the majority (79 per cent) of pulsators to be below this threshold. However, upon closer inspection, the ΔRV distribution of pulsators (top panel of Fig. 7) consists of three peaks and a long tail to large values. For example, a 20 km s^{-1} threshold fails to capture all of stars in the second peak ($10 \lesssim \Delta RV \lesssim 25$ km s^{-1}) nor any of the stars in the third peak ($25 \lesssim \Delta RV \lesssim 40$ km s^{-1}) in the distribution. We observe a non-negligible fraction of pulsators with ΔRV > 20 km s^{-1} and an extended tail that reaches as high as 100 km s^{-1}. On the other hand, when considering only the non-pulsating stars (in the bottom panel of Fig. 7), we find a far fewer systems with ΔRV > 20 km s^{-1} in absolute numbers but also a smaller relative fraction of the whole sample.

To demonstrate the efficacy and validity of the C = 20 km s^{-1} threshold with respect to how pulsations among binary candidates can create false positives, we compare in Fig. 8 the calculated ΔRV values of each star to the highest-amplitude pulsation as measured in time-series TESS photometry. For the latter, we only considered frequencies larger than 1 d^{-1} in an attempt to avoid including any periodicity potentially related to rotation. For visibility, we have added a dashed-grey unity line to Fig. 8, which represents that a spectroscopic pulsation amplitude of ΔRV = 1 km s^{-1} would be equivalent to a photometric amplitude of 1 mmag. Globally, we observe that the different pulsator types approximately follow the same trend, albeit with a lot of scatter, and no single pulsator type is over-represented in any one region of the parameter space. Calculating the Pearson correlation coefficients for each pulsator class, we get values of −0.039, −0.038, and −0.042, for the populations of β Cep, SPB, and SLF respectively. The considerable scatter in Fig. 8 demonstrates that a single threshold of C = 20 km s^{-1} for galactic B-type stars applied without any knowledge of the pulsation RV distribution may lead to mis-classification of high-amplitude pulsators as binaries and vice versa, in alignment with the findings of Simón-Díaz et al. (2024).

On balance, the choice of 20 km s^{-1} as a threshold seems reasonable for a large sample of galactic massive stars that contains a large fraction of pulsators. But there is a need for considerable caution for applying such a criterion blindly with no knowledge of the underlying pulsation fraction and as a consequence the pulsation-induced RV distribution. With additional spectroscopic epochs, we would expect the median ΔRV value to increase as both additional pulsators and binaries are identified. On the other hand, shifting the ΔRV threshold to larger values would decrease the number of false binary positives, but would also increase the number of false binary negatives. This is because genuine binaries are more likely to not be classified as a binary if using a higher RV threshold. Therefore, we conclude that an informed investigation of photometric pulsation periods in parallel to spectroscopic binary periods is highly advisable for studies of galactic massive stars (see also Nardini et al. in prep). In this way, an optimum choice of threshold can be made since it would be informed by photometric constraints on the amplitudes and periods of pulsations. Additionally, when considering the results of the various studies investigating binary fractions for a range of sample sizes and types found in the literature, a single threshold value seems unable to take into account the full breadth of variability observed within the populations of O- and B-type stars and that, following the conclusions of Simón-Díaz et al. (2024), one should rather consider multiple thresholds based on a given star's position in the HR diagram.

6 ROTATIONAL MODULATION

Rotational modulation is the periodic variation in stellar brightness caused by non-uniform surface features, such as chemical spots resulting from the presence of a large-scale magnetic field (e.g. Stibbs 1950). Since the chemical spots of early-type stars are long-lived, the photometric signature of rotational modulation is a series of harmonics in the LS periodogram with the base frequency being the rotation frequency (e.g. Bowman et al. 2018; Mathys et al. 2020). Previous studies have yielded success rates between 50 and 70 per cent for the detection of magnetic fields via spectropolarimetry for stars with chemical spots inferred from rotational modulation (e.g. Buysschaert et al. 2018a). Rotational modulation also has the added benefit of being applicable to a wide range of spectral types, as compared to chemical peculiarity, whose features and causes can vary between spectral types (see Preston 1974).

Based on all available TESS light curves for our sample and the associated frequency spectra, we searched for rotational modulation. We define a star to have rotational modulation if at least one harmonic of an isolated low-frequency signal is present in the frequency spec-

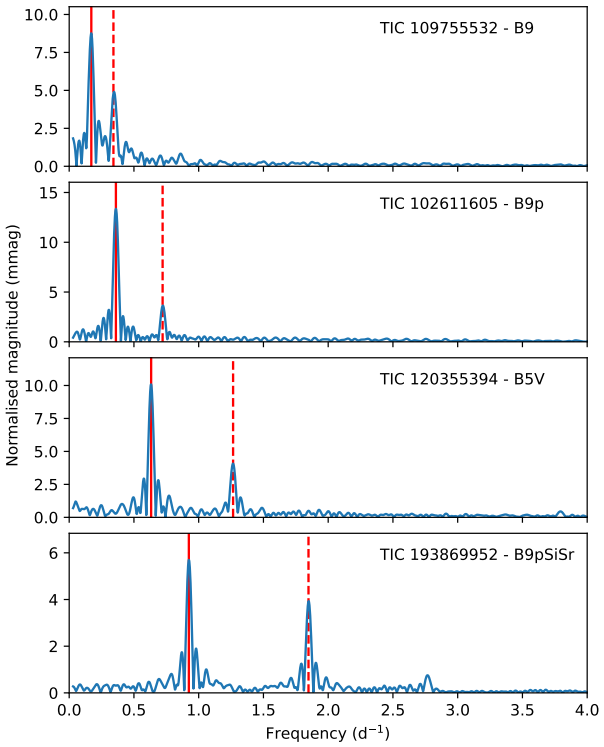

Figure 9. LS periodograms for four example stars showing rotational modulation. In each case, the solid red line corresponds to the rotation frequency, and the dashed red line corresponds to its first harmonic ($f = 2 \times f_{\rm rot}$). The TIC ID of each star and its SIMBAD spectral type is shown in the top-right corner of each panel.

trum (i.e. two harmonically-related frequencies). A few examples of such stars with rotational modulation are shown in Fig. 9. Using this criterion, we identify 148 stars in our sample with rotational modulation. This subset of stars may show multiple forms of variability, such as pulsating stars that also present rotational modulation, and is not necessarily these star's dominant form of variability. Therefore, these 148 stars with rotational modulation are worthy of follow-up spectropolarimetry to search for the presence of a large-scale surface magnetic field.

Of particular interest are candidate magnetic stars with pulsations, since these are prime targets for magneto-asteroseismology (see Buysschaert et al. 2018b; Lecoanet et al. 2022). We identify 15 SPB and 16 β Cep stars showing rotational modulation. Although a modest sample in terms of size, we shall perform an in-depth investigation of these stars in a future work.

7 CONCLUSIONS

We have combined multi-epoch high-resolution spectra from a dedicated large programme with the HERMES spectrograph mounted on the Mercator telescope with new 2-min cadence TESS photometry to investigate the ensemble properties of a large sample of 873 galactic O- and B-type stars. In particular, we focus on spectroscopic and photometric signatures of pulsations, binarity, and rotational modulation as a potential indicator for magnetism. This much larger sample of Northern massive stars complements the previous study by Burssens et al. (2020), which was focussed on the Southern hemisphere.

We demonstrate that the vast majority of massive galactic stars are pulsators, with a diversity of pulsations allowing us to identify β Cep stars, SPB stars, and SLF variability. In general, photometric variability amongst massive stars appears to be nearly ubiquitous, with only 58 of the 873 stars in our sample showing no significant variability at all (i.e. constant stars). These 58 stars are all B-type stars but have a range of luminosity classes. With longer TESS light curves and/or improved photometric precision, it is not impossible that many of these would be detected as photometrically variable as well. As part of our ensemble analysis, we have determined the empirical locations of the β Cep, SPB and SLF variability in the HR diagram as the parameter space in which the 33rd and 66th percentile of stars show a specific type of variability. The stellar evolution tracks and corresponding theoretical instability regions for p and g modes used in this work originate from Burssens et al. (2020), but assume a single set of physical prescriptions. Hence, these theoretical predictions do not capture changes in the location of the TAMS because of different mixing processes, nor differences caused by metallicity, rotation, or magnetism. Yet, the location of pulsating stars agrees fairly well with expectations. Most importantly, we have used the empirical instability regions of these three pulsator types to demonstrate that CBM is likely mass dependent (e.g. Scott et al. 2021; Whitehead et al. 2026), especially above $M \gtrsim 15$ M$_\odot$.

Our multi-epoch HERMES spectra allowed us to identify 82 spectroscopic binaries, including 19 SB2 systems. We also identify the photometric signatures of binarity and discover 30 new eclipsing binaries, with 12 of them containing a β Cep or SPB pulsator and 11 of them having SLF variability. We investigated the impact of the choice of RV threshold for identifying spectroscopic binary systems. We find that a non-negligible fraction of single pulsating stars have pulsation amplitudes larger than the typically used threshold of 20 km s^{-1} for determining significant RV variability presumed to be caused by binarity. Whilst O-type stars in low-metallicity environments, such as the LMC and SMC galaxies, are typically not high-amplitude pulsators, this is not the case of galactic B-type stars. The distribution of pulsation amplitudes for galactic (single) B-type stars peaks at around 20 km s^{-1} and has an extended tail that reaches upwards of 40 km s^{-1}. In our sample, we have the advantage of being able to directly compare the spectroscopic RV amplitudes and photometric amplitudes, thus providing additional insight into being able to distinguish between one source of RV variability from another when using a threshold of 20 km s^{-1}. Therefore, given the availability of TESS data across the entire sky, we advocate that spectroscopic studies of binarity among galactic massive stars should be informed by photometry. Unfortunately, the number of spectroscopic epochs for most stars in our sample is limited, and so a full binary analysis is not possible, but we have identified systems worthy of follow-up.

In addition, we identify 148 stars with rotational modulation in their TESS light curves, which is a proven indicator of a potential large-scale strong magnetic field for early-type stars (e.g. Buysschaert et al. 2018a; Shultz et al. 2019). We also identify 39 pulsating stars with rotational modulation, which may have strong, large-scale magnetic fields making them potential targets for magneto-asteroseismology. The inclusion of magnetic fields in a forward asteroseismic modelling framework yields more robust insight into the rotation and mixing properties of magnetic stars.

In the future, we will perform forward asteroseismic modelling of individual targets that have been characterised as high-priority from this work to calibrate the physical prescriptions of mixing in stellar structure and evolution models. While individual TESS sectors are usually sufficient to distinguish pulsator types, they are typically not sufficient for performing precise mode identification (see Scott & Bowman 2026). The ideal scenario is, therefore, to have

multiple consecutive sectors of TESS data, which is only realised for a fraction of our sample. Massive stars were generally avoided by the Kepler mission, and the light curves assembled by the K2 and TESS missions are, on average, quite short for robust forward asteroseismic modelling. However, we expect long-duration, short-cadence, and high-precision photometric precision light curves from the ESA PLATO mission (Rauer et al. 2025), which is scheduled to be launched in early-2027. Thanks to PLATO's observing strategy, a long temporal baseline of at least 2 yr will enable pulsation mode identification for many massive stars. Our current study demonstrates that the asteroseismic return of studying massive stars with TESS data is very high, hence an equally high return is expected for massive stars observed by the PLATO mission. Combining these TESS photometric data with other observing techniques, such as spectroscopy and spectropolarimetry, we will form a more complete picture of how massive stars evolve and interact with their companions.

ACKNOWLEDGEMENTS

This research has made use of the SIMBAD database operated at CDS, Strasbourg (France), and of NASA's Astrophysics Data System (ADS).

Based on observations made with the Mercator Telescope (https://www.mercator.iac.es), operated on the island of La Palma by the Flemish Community, at the Spanish Observatorio del Roque de los Muchachos of the Instituto de Astrofísica de Canarias, and obtained with the HERMES spectrograph, which is supported by the Research Foundation - Flanders (FWO), Belgium, the Research Council of KU Leuven, Belgium, the Fonds National de la Recherche Scientifique (F.R.S.-FNRS), Belgium, the Royal Observatory of Belgium, the Observatoire de Genève, Switzerland and the Thüringer Landessternwarte Tautenburg, Germany. The authors thank the Institute of Astronomy (KU Leuven) and the many observers which contributed to the data gathering.

This paper includes data assembled by the TESS mission, with funding for the TESS mission provided by NASA's Science Mission directorate. This work used data from the European Space Agency (ESA) mission Gaia (https://www.cosmos.esa.int/gaia), processed by the Gaia Data Processing and Analysis Consortium (DPAC; https://www.cosmos.esa.int/web/gaia/dpac/consortium). Funding for the DPAC of the Gaia mission is provided by national institutions, in particular the institutions participating in the Gaia Multilateral Agreement.

The authors gratefully acknowledge UK Research and Innovation (UKRI) in the form of a Frontier Research grant under the UK government's ERC Horizon Europe funding guarantee (SYMPHONY; PI Bowman; grant number: EP/Y031059/1), and a Royal Society University Research Fellowship (PI Bowman; grant number: URF\R1\231631). This project received support from the "La Caixa" Foundation (ID 100010434) under the fellowship code LCF/BQ/PI23/11970035. JB is supported by an NWO Veni fellowship (VI.Veni.242.199). GH thanks the Polish National Center for Science (NCN) for support through grant 2021/43/B/ST9/02972. N.S. and I.A. acknowledge support from the Israel Science Foundation (grant number 2752/19) and from the Pazy foundation (grant number 216312). I.A. acknowledges further support from the European Research Council (ERC) under the European Union's Horizon 2020 research and innovation program (grant agreement number 852097). TS acknowledges support from the Israel Science Foundation (ISF) under grant number 0603225041 and from the European Research Council (ERC) under the European Union's Horizon 2020 research and innovation program (grant agreement 101164755/METAL). S.S-D. acknowledges support from the State Research Agency (AEI) of the Spanish Ministry of Science and Innovation (MICIN) and the European Regional Development Fund, FEDER under grants PRODUCTOS DE LA INTERACCION DE ESTRELLAS MASIVAS REVELADOS POR GRANDES SONDEOS ESPECTROSCOPICOS, with reference PID2024-159329NB-C21. S.S-D. also acknowledge funding from European Commission (EC) under Project OCEANS - Overcoming challenges in the evolution and nature of massive stars, HORIZON-MSCA-2023-SE-01, No G.A 101183150 Funded by the European Union. Views and opinions expressed are however those of the author(s) only and do not necessarily reflect those of the European Union or the European Research Executive Agency (REA). Neither the European Union nor the granting authority can be held responsible for them.

DATA AVAILABILITY

The TESS data used in this work are publicly available via the MAST website: https://archive.stsci.edu/missions-and-data/tess. The GAIA data used in this work are publicly available via the Gaia website: https://gea.esac.esa.int/archive/, processed by the Gaia Data Processing and Analysis Consortium (DPAC; https://www.cosmos.esa.int/web/gaia/dpac/consortium). This research has made use of the following open-access software packages: `TLUSTY` for the grids of synthetic spectra (Lanz & Hubeny 2003, 2007), `LIGHTKURVE` (https://lightkurve.github.io/lightkurve/), a `PYTHON` package for *Kepler* and TESS data analysis (Lightkurve Collaboration 2018), `PERIOD04` (https://www.period04.net) for frequency analysis (Lenz & Breger 2005), as well as `matplotlib` (Hunter 2007), `numpy` (Harris et al. 2020), `astropy` (Astropy Collaboration et al. 2013b, 2018b, 2022), and `scipy` (Virtanen et al. 2020).

For the purpose of open access, the authors have applied a CC BY licence to the author accepted manuscript version: https://arxiv.org/abs/TBD. Data products that support the results in this paper are publicly available via the Zenodo repository: https://zenodo.org/records/TBD.

REFERENCES

Abbott B. P., et al., 2017a, Nature, 551, 85
Abbott B. P., et al., 2017b, ApJ, 848, L12
Aerts C., 2021, Reviews of Modern Physics, 93, 015001
Aerts C., Rogers T. M., 2015, ApJ, 806, L33
Aerts C., Puls J., Godart M., Dupret M. A., 2009, A&A, 508, 409
Aerts C., Christensen-Dalsgaard J., Kurtz D. W., 2010, Asteroseismology. Springer, doi:10.1007/978-1-4020-5803-5
Aerts C., Mathis S., Rogers T. M., 2019, ARA&A, 57, 35
Anders E. H., et al., 2023, Nature Astronomy, 7, 1228
Astropy Collaboration et al., 2013a, A&A, 558, A33
Astropy Collaboration et al., 2013b, A&A, 558, A33
Astropy Collaboration et al., 2018a, AJ, 156, 123
Astropy Collaboration et al., 2018b, AJ, 156, 123
Astropy Collaboration et al., 2022, ApJ, 935, 167
Auvergne M., et al., 2009, A&A, 506, 411
Avvakumova E. A., Malkov O. Y., Kniazev A. Y., 2013, Astronomische Nachrichten, 334, 860
Bailer-Jones C. A. L., et al., 2013, A&A, 559, A74
Banyard G., Sana H., Mahy L., Bodensteiner J., Villaseñor J. I., Evans C. J., 2022, A&A, 658, A69

Blomme R., et al., 2011, A&A, 533, A4
Bodensteiner J., et al., 2021, A&A, 652, A70
Bodensteiner J., et al., 2023, A&A, 680, A32
Bodensteiner J., et al., 2025, A&A, 698, A38
Borucki W. J., et al., 2010, Science, 327, 977
Bowman D. M., 2020, Frontiers in Astronomy and Space Sciences, 7, 70
Bowman D. M., 2023, Ap&SS, 368, 107
Bowman D. M., Dorn-Wallenstein T. Z., 2022, A&A, 668, A134
Bowman D. M., Buysschaert B., Neiner C., Pápics P. I., Oksala M. E., Aerts C., 2018, A&A, 616, A77
Bowman D. M., et al., 2019a, Nature Astronomy, 3, 760
Bowman D. M., Johnston C., Tkachenko A., Mkrtichian D. E., Gunsriwiwat K., Aerts C., 2019b, ApJ, 883, L26
Bowman D. M., Burssens S., Simón-Díaz S., Edelmann P. V. F., Rogers T. M., Horst L., Röpke F. K., Aerts C., 2020, A&A, 640, A36
Bowman D. M., et al., 2022, A&A, 658, A96
Bowman D. M., Van Daele P., Michielsen M., Van Reeth T., 2024, A&A, 692, A49
Brasseur C. E., Phillip C., Fleming S. W., Mullally S. E., White R. L., 2019, Astrocut: Tools for creating cutouts of TESS images, Astrophysics Source Code Library, record ascl:1905.007
Britavskiy N., et al., 2025, A&A, 698, A40
Bromm V., Larson R. B., 2004, ARA&A, 42, 79
Burssens S., et al., 2020, A&A, 639, A81
Burssens S., et al., 2023, Nature Astronomy, 7, 913
Buysschaert B., Neiner C., Martin A. J., Aerts C., Bowman D. M., Oksala M. E., Van Reeth T., 2018a, MNRAS, 478, 2777
Buysschaert B., Aerts C., Bowman D. M., Johnston C., Van Reeth T., Pedersen M. G., Mathis S., Neiner C., 2018b, A&A, 616, A148
Cantiello M., Lecoanet D., Jermyn A. S., Grassitelli L., 2021, ApJ, 915, 112
Castro N., Fossati L., Langer N., Simón-Díaz S., Schneider F. R. N., Izzard R. G., 2014, A&A, 570, L13
Chaplin W. J., Miglio A., 2013, ARA&A, 51, 353
Chen X., et al., 2022, ApJS, 263, 34
Cui X.-Q., et al., 2012, RAA, 12, 1197
Dsilva K., Shenar T., Sana H., Marchant P., 2020, A&A, 641, A26
Dunstall P. R., et al., 2015, A&A, 580, A93
Edelmann P. V. F., Ratnasingam R. P., Pedersen M. G., Bowman D. M., Prat V., Rogers T. M., 2019, ApJ, 876, 4
Ekström S., et al., 2012, A&A, 537, A146
Erba C., et al., 2024, ApJ, 977, 84
Eze C. I., Handler G., 2024, ApJS, 272, 25
Fouesneau M., et al., 2023, A&A, 674, A28
Fritzewski D. J., Vanrespaille M., Aerts C., Guo Z., Hey D., De Ridder J., 2025, A&A, 698, A253
Frost A. J., et al., 2025, A&A, 701, A171
Gaia Collaboration et al., 2023a, A&A, 674, A1
Gaia Collaboration et al., 2023b, A&A, 674, A39
Gilkis A., Shenar T., Ramachandran V., Jermyn A. S., Mahy L., Oskinova L. M., Arcavi I., Sana H., 2021, MNRAS, 503, 1884
Gray D. F., 2005, The Observation and Analysis of Stellar Photospheres, third edn. Cambridge University Press
Handler G., 2009, Communications in Asteroseismology, 159, 42
Harris C. R., et al., 2020, Nature, 585, 357
Hekker S., Christensen-Dalsgaard J., 2017, A&ARv, 25, 1
Hey D., Aerts C., 2024, A&A, 688, A93
Hubeny I., Lanz T., 1995, ApJ, 439, 875
Hunter J. D., 2007, Computing in Science & Engineering, 9, 90
IJspeert L. W., Tkachenko A., Johnston C., Garcia S., De Ridder J., Van Reeth T., Aerts C., 2021, A&A, 652, A120
Jenkins J. M., et al., 2016, in Chiozzi G., Guzman J. C., eds, Society of Photo-Optical Instrumentation Engineers (SPIE) Conference Series Vol. 9913, Software and Cyberinfrastructure for Astronomy IV. p. 99133E, doi:10.1117/12.2233418
Kalita A. J., Bowman D. M., Abdul-Masih M., Simón-Díaz S., 2025, A&A, 703, A2
Krtička J., Feldmeier A., 2018, A&A, 617, A121
Krtička J., Feldmeier A., 2021, A&A, 648, A79
Kurtz D. W., 2022, ARA&A, 60, 31
Langer N., 2012, ARA&A, 50, 107
Langer N., Kudritzki R. P., 2014, A&A, 564, A52
Lanz T., Hubeny I., 2003, ApJS, 146, 417
Lanz T., Hubeny I., 2007, ApJS, 169, 83
Laplace E., Götberg Y., de Mink S. E., Justham S., Farmer R., 2020, A&A, 637, A6
Lecoanet D., Bowman D. M., Van Reeth T., 2022, MNRAS, 512, L16
Lenz P., Breger M., 2005, Communications in Asteroseismology, 146, 53
Lightkurve Collaboration et al., 2018, Lightkurve: Kepler and TESS time series analysis in Python, Astrophysics Source Code Library, record ascl:1812.013
Lomb N. R., 1976, Ap&SS, 39, 447
Mahy L., et al., 2022, A&A, 657, A4
Malkov O. Y., Oblak E., Snegireva E. A., Torra J., 2006, A&A, 446, 785
Marchant P., Bodensteiner J., 2024, ARA&A, 62, 21
Martins F., Palacios A., 2013, A&A, 560, A16
Massey P., 2003, ARA&A, 41, 15
Mathys G., Kurtz D. W., Holdsworth D. L., 2020, A&A, 639, A31
Merle T., et al., 2026, MNRAS, 547, stag351
Meynet G., Maeder A., 2000, A&A, 361, 101
Moe M., Di Stefano R., 2017, ApJS, 230, 15
Moravveji E., 2016, MNRAS, 455, L67
Mowlavi N., et al., 2023, A&A, 674, A16
Nardini F., Bodensteiner J., Sana H., Mahy L., Deshmukh K., Bowman D. M., 2025, MNRAS, 540, 2009
Nieva M. F., Przybilla N., 2012, A&A, 539, A143
Offner S. S. R., Moe M., Kratter K. M., Sadavoy S. I., Jensen E. L. N., Tobin J. J., 2023, in Inutsuka S., Aikawa Y., Muto T., Tomida K., Tamura M., eds, Astronomical Society of the Pacific Conference Series Vol. 534, Protostars and Planets VII. p. 275 (arXiv:2203.10066), doi:10.48550/arXiv.2203.10066
Pathak P., Blouin S., Herwig F., Woodward P. R., 2025, arXiv e-prints, p. arXiv:2508.03893
Pavlovski K., Southworth J., 2009, MNRAS, 394, 1519
Paxton B., Bildsten L., Dotter A., Herwig F., Lesaffre P., Timmes F., 2011, ApJS, 192, 3
Paxton B., et al., 2013, ApJS, 208, 4
Paxton B., et al., 2015, ApJS, 220, 15
Paxton B., et al., 2018, ApJS, 234, 34
Paxton B., et al., 2019, ApJS, 243, 10
Pedersen M. G., 2022, ApJ, 940, 49
Pedersen M. G., Bildsten L., 2025, MNRAS, 539, 2742
Pedersen M. G., Escorza A., Pápics P. I., Aerts C., 2020, MNRAS, 495, 2738
Pedersen M. G., et al., 2021, Nature Astronomy, 5, 715
Pourbaix D., et al., 2004, A&A, 424, 727
Preston G. W., 1974, ARA&A, 12, 257
Prša A., et al., 2022, ApJS, 258, 16
Raskin G., Van Winckel H., 2014, Astronomische Nachrichten, 335, 32
Raskin G., et al., 2011, A&A, 526, A69
Rauer H., et al., 2025, Experimental Astronomy, 59, 26
Ricker G. R., et al., 2015, J. Astron. Telesc. Instrum. Syst., 1, 014003
Rogers T. M., McElwaine J. N., 2017, ApJ, 848, L1
Rogers T. M., Lin D. N. C., McElwaine J. N., Lau H. H. B., 2013, ApJ, 772, 21
Różański T., Niemczura E., Lemiesz J., Posiłek N., Różański P., 2022, A&A, 659, A199
Sana H., et al., 2012, Science, 337, 444
Sana H., et al., 2013, A&A, 550, A107
Sana H., et al., 2025, Nature Astronomy, 9, 1337
Scargle J. D., 1982, ApJ, 263, 835
Schultz W. C., Bildsten L., Jiang Y.-F., 2022, ApJ, 924, L11
Scott L. J. A., Bowman D. M., 2026, MNRAS, 545, staf2174
Scott L. J. A., Hirschi R., Georgy C., Arnett W. D., Meakin C., Kaiser E. A., Ekström S., Yusof N., 2021, MNRAS, 503, 4208
Shenar T., et al., 2019, A&A, 627, A151
Shultz M. E., et al., 2019, MNRAS, 490, 274
Simón-Díaz S., Herrero A., 2014, A&A, 562, A135

Simón-Díaz S., Godart M., Castro N., Herrero A., Aerts C., Puls J., Telting J., Grassitelli L., 2017, A&A, 597, A22
Simón-Díaz S., Britavskiy N., Castro N., Holgado G., de Burgos A., 2024, arXiv e-prints, p. arXiv:2405.11209
Southworth J., Bowman D. M., 2022, MNRAS, 513, 3191
Southworth J., Bowman D., 2025, arXiv e-prints, p. arXiv:2509.08426
Southworth J., Bowman D. M., Tkachenko A., Pavlovski K., 2020, MNRAS, 497, L19
Stankov A., Handler G., 2005, ApJS, 158, 193
Stibbs D. W. N., 1950, MNRAS, 110, 395
Szewczuk W., Daszyńska-Daszkiewicz J., 2017, MNRAS, 469, 13
Temaj D., Schneider F. R. N., Laplace E., Wei D., Podsiadlowski P., 2024, A&A, 682, A123
Thompson W., Herwig F., Woodward P. R., Mao H., Denissenkov P., Bowman D. M., Blouin S., 2024, MNRAS, 531, 1316
Thomson-Paressant K., Neiner C., Labadie-Bartz J., Ouazzani R.-M., Mathis S., Manchon L., 2025, A&A, 704, A134
Townsend R. H. D., 2005, MNRAS, 364, 573
Townsend R. H. D., Teitler S. A., 2013, MNRAS, 435, 3406
Townsend R. H. D., Goldstein J., Zweibel E. G., 2018, MNRAS, 475, 879
Vanlaer V., Bowman D. M., Burssens S., Bharati Das S., Bugnet L., Mathis S., Aerts C., 2025, A&A, 701, A5
Villaseñor J. I., et al., 2025, A&A, 698, A41
Vink J. S., de Koter A., Lamers H. J. G. L. M., 2001, A&A, 369, 574
Virtanen P., et al., 2020, Nature Methods, 17, 261
Wenger M., et al., 2000, A&AS, 143, 9
Whitehead E. E., Hirschi R., Varma V., Mueller B., Rizzuti F., Georgy C., Arnett W. D., 2026, MNRAS, 546, staf2245
Xiang M., et al., 2022, A&A, 662, A66
Zapartas E., et al., 2026, MNRAS, 546, staf2208
Zhao G., Zhao Y.-H., Chu Y.-Q., Jing Y.-P., Deng L.-C., 2012, RAA, 12, 723
Zucker S., Mazeh T., Santos N. C., Udry S., Mayor M., 2003, A&A, 404, 775
de Burgos A., Simón-Díaz S., Urbaneja M. A., Holgado G., Ekström S., Ramírez-Tannus M. C., Zari E., 2025, A&A, 695, A87
de Mink S. E., Langer N., Izzard R. G., Sana H., de Koter A., 2013, ApJ, 764, 166

APPENDIX A: COMPARISON OF CONTINUUM NORMALISATION TECHNIQUE

In Fig. A1, we show a comparison of the best-fitting TLUSTY models derived from the manually normalised and SUPPNET-normalised HERMES spectra, for a selection of stars. This comparison, which is typical for the entire sample, demonstrates the excellent result of SUPPNET, since the difference in $T_{\rm eff}$ and $\log\ g$ values between each best-fitting model is usually a maximum of one grid step size.

APPENDIX B: NEW ECLIPSING BINARY LIGHT CURVES

In Figs. B1–B5, we show TESS light curves of all the new EBs that have been discovered in this work.

This paper has been typeset from a TEX/LATEX file prepared by the author.

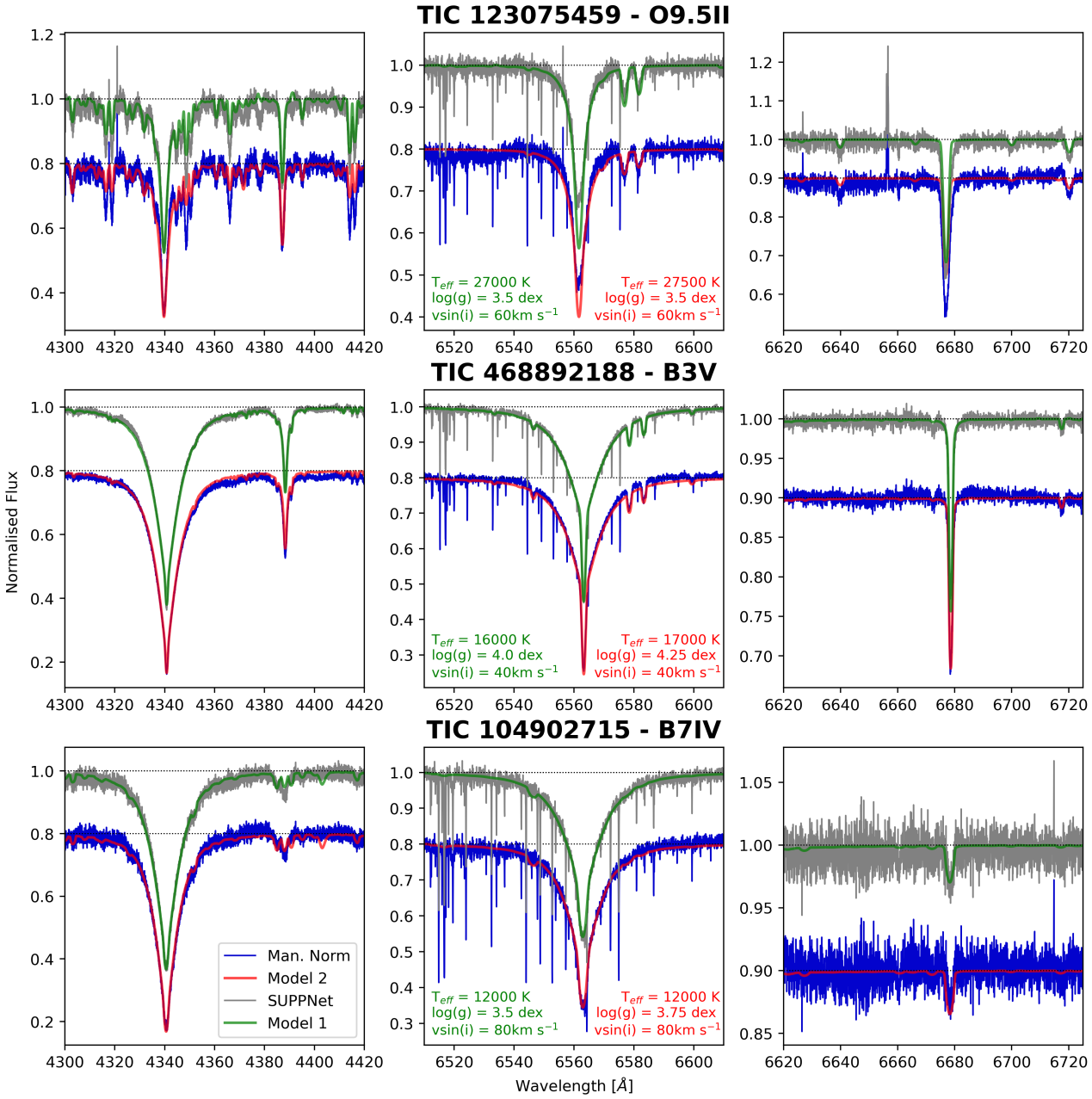

Figure A1. Comparison of the results of normalisation between manual (blue) and via SUPPNet (grey) for three representative stars. The resultant best-fitting TLUSTY models are shown in red and green, respectively, and the best-fitting parameters of each solution are shown in same colour in the middle panel for each row. A dashed line has been added to each spectrum to show the continuum level.

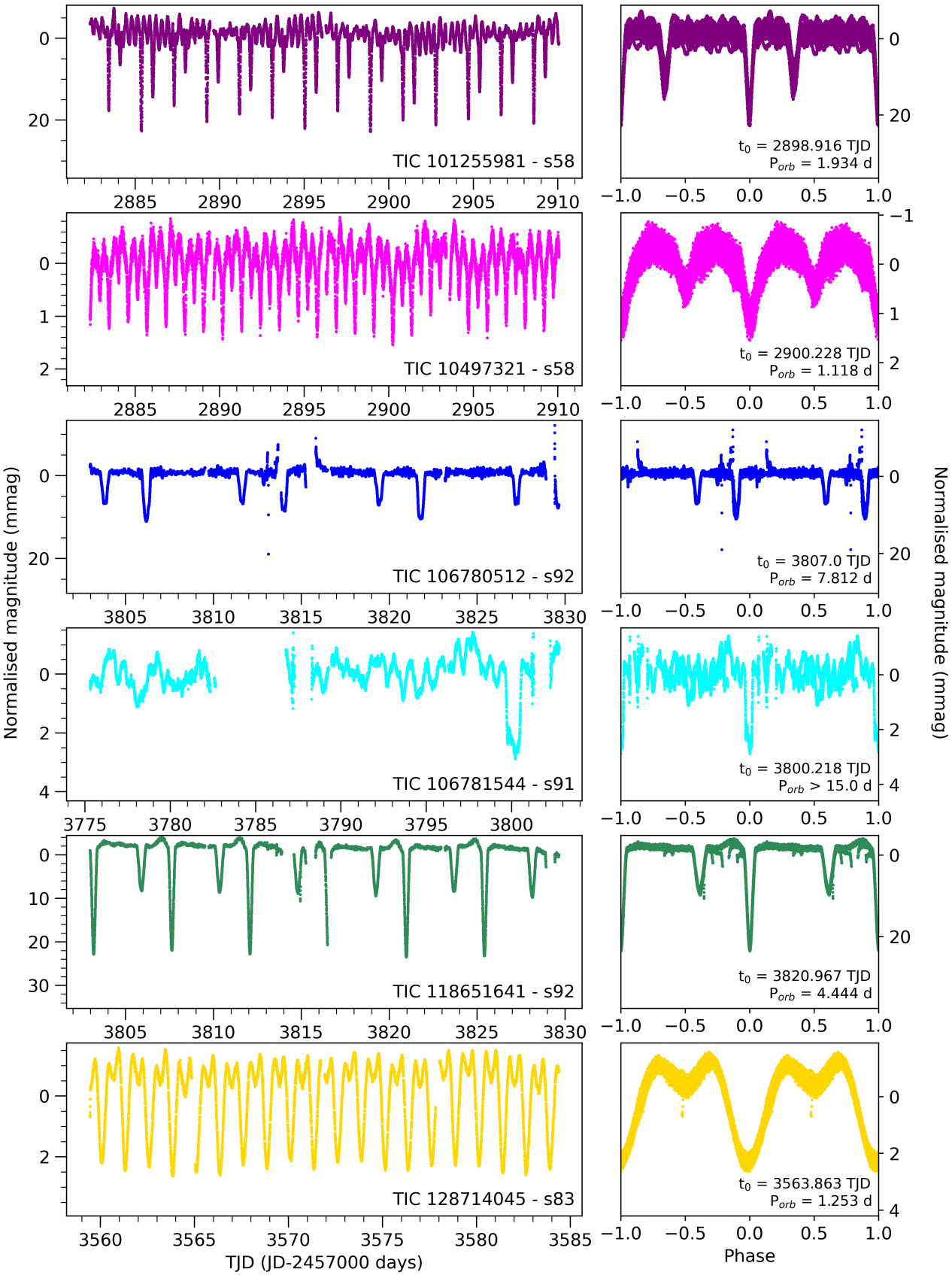

Figure B1. Left: Light curves for the 30 new EBs identified through this work, with their TIC ID and respective sector number. Right: Phase-folded light curves, with the corresponding orbital period P_{orb} and reference time T_0 based on the primary eclipse.

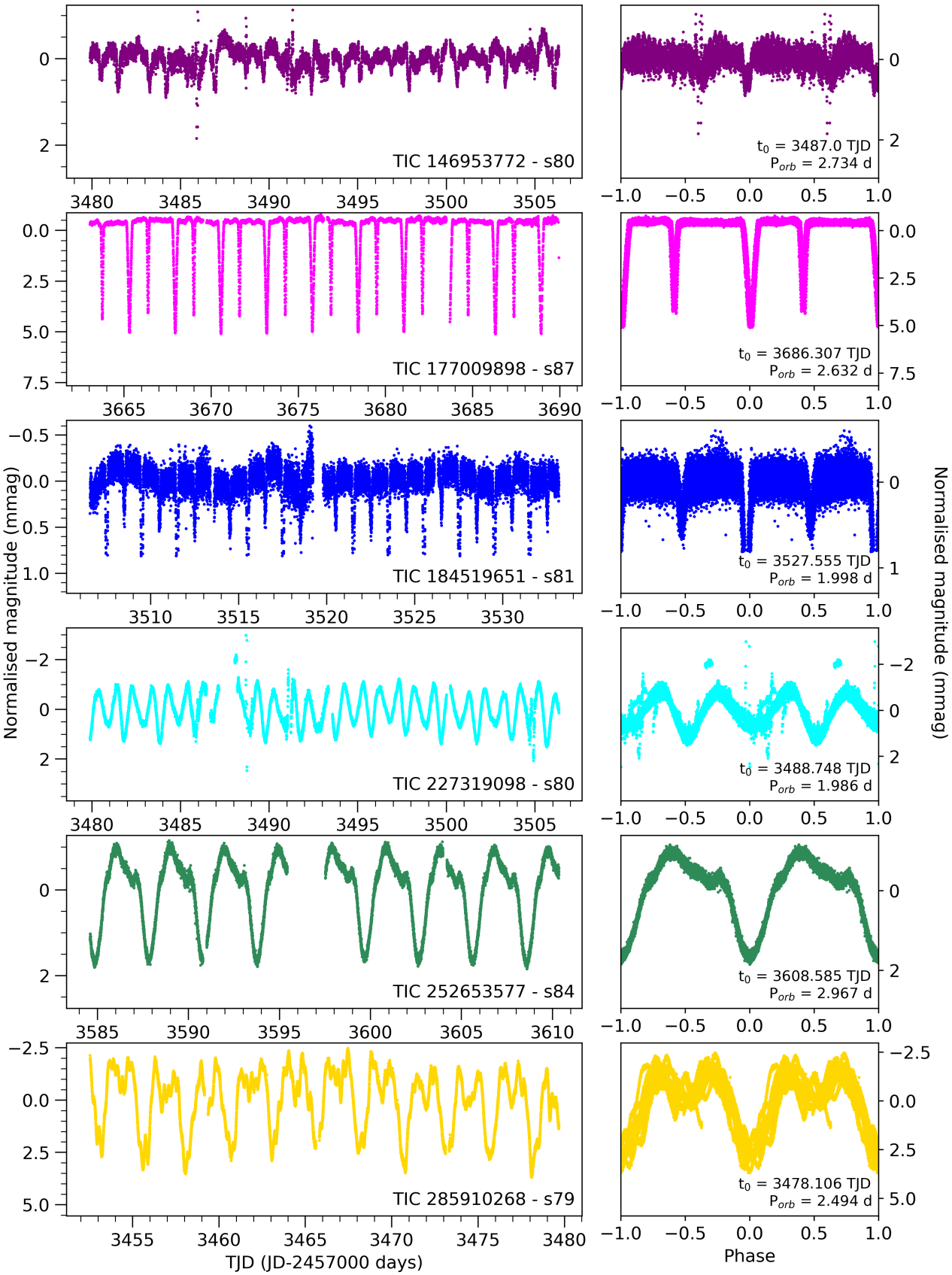

Figure B2. Same as Fig. B1 (continued.).

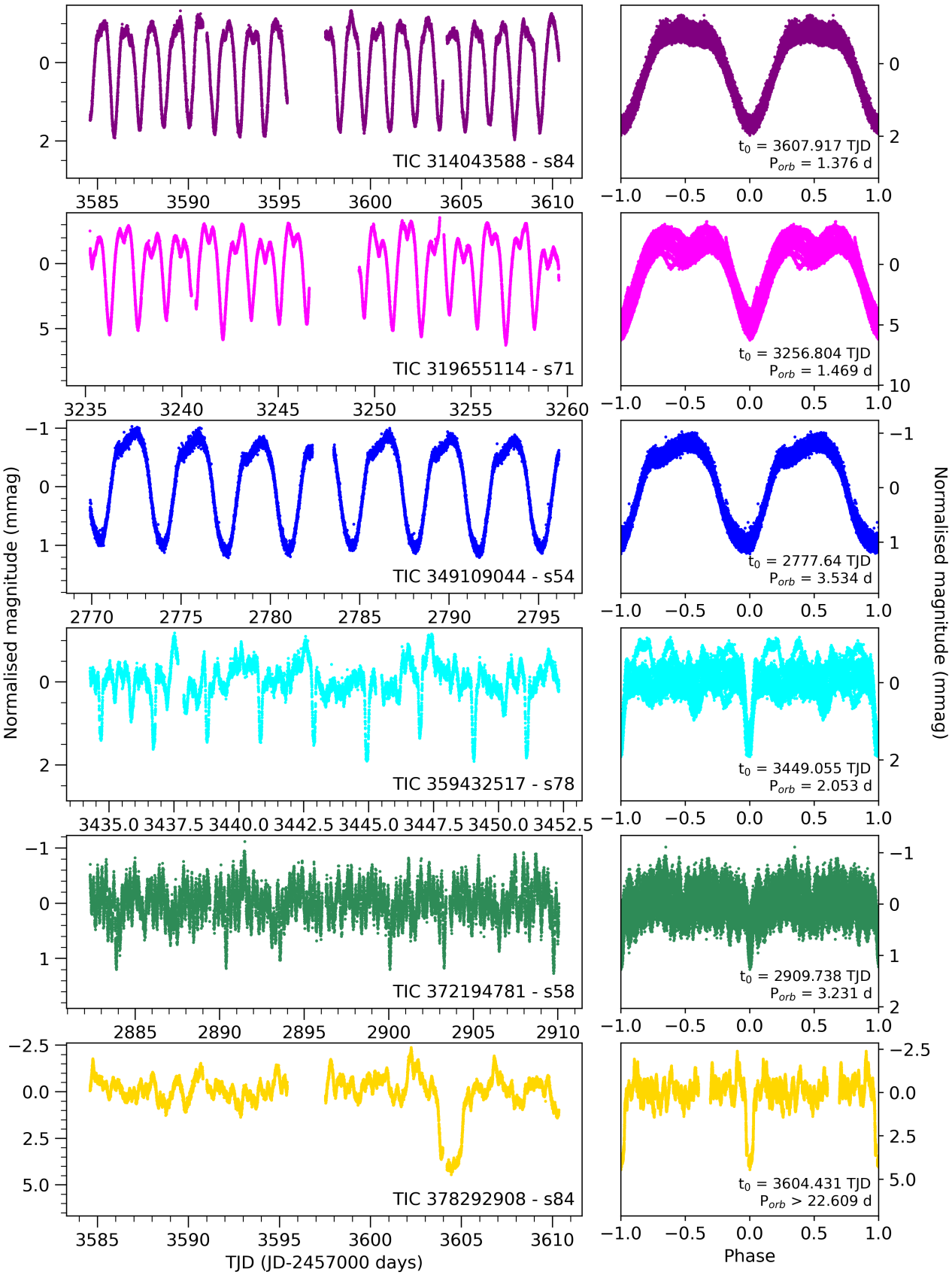

Figure B3. Same as Fig. B1 (continued.).

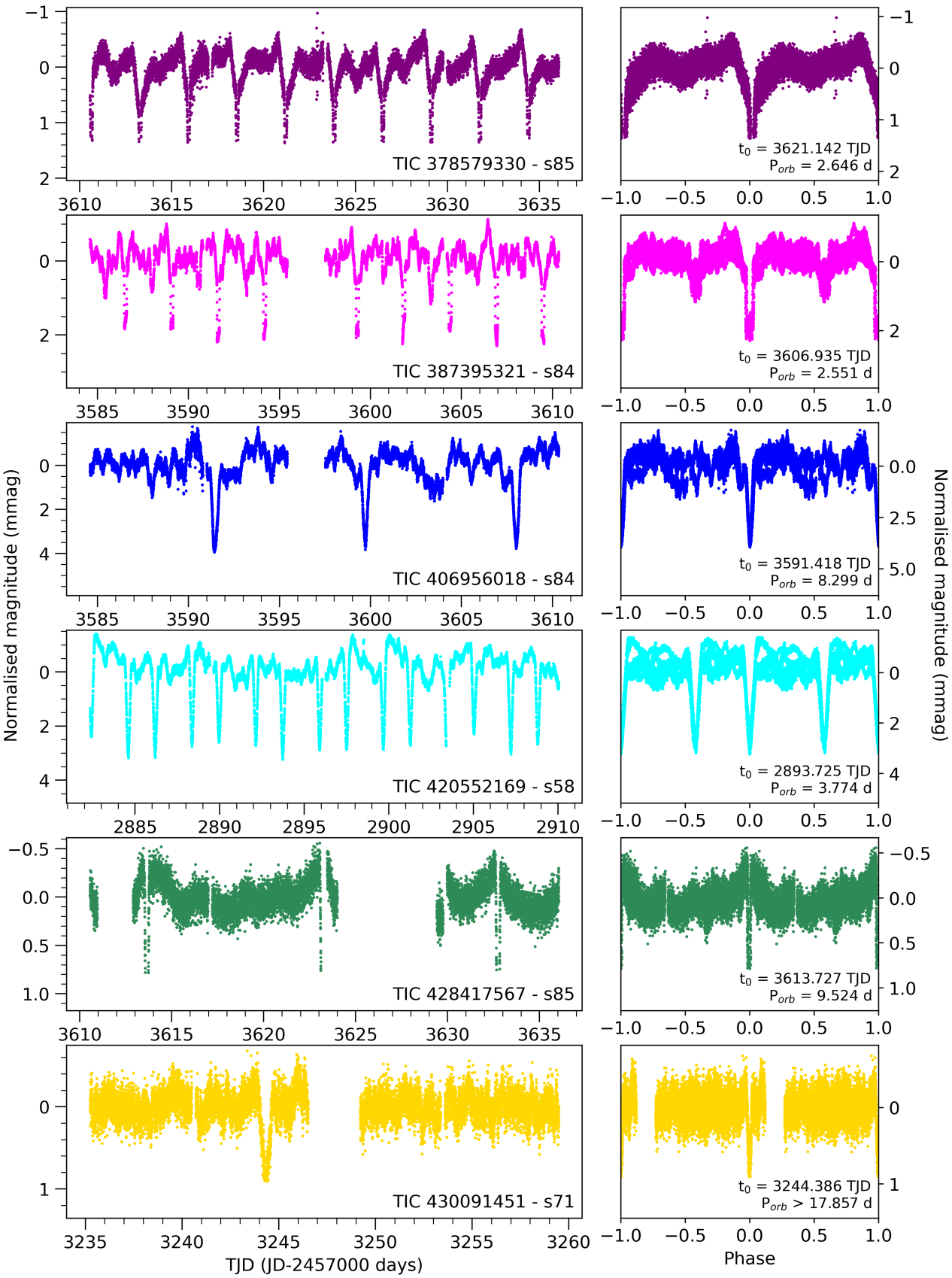

Figure B4. Same as Fig. B1 (continued.).

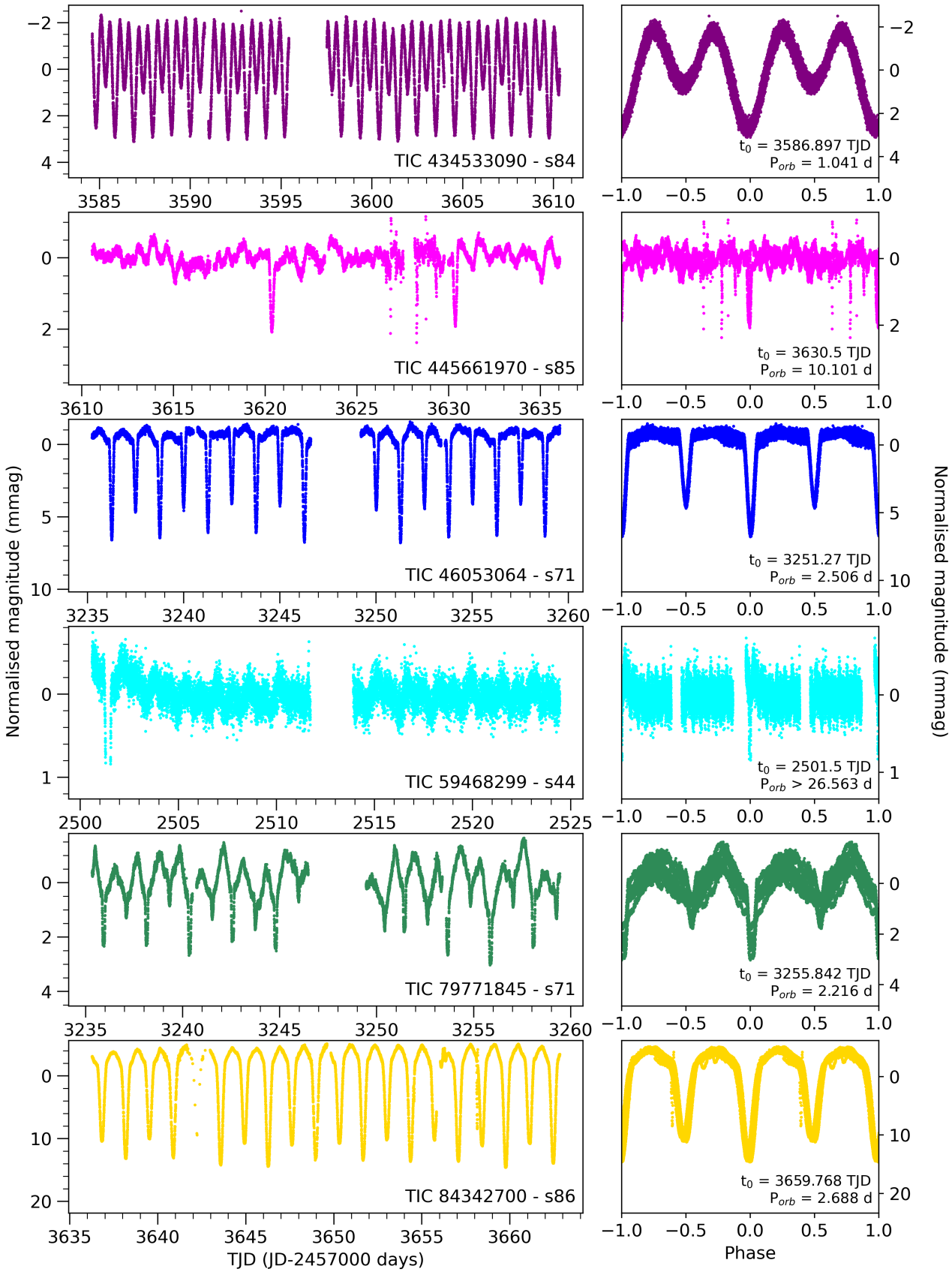

Figure B5. Same as Fig. B1 (continued.).